J. Fluid Mech. (2024), *vol*. 986, A23, doi:10.1017/jfm.2024.340

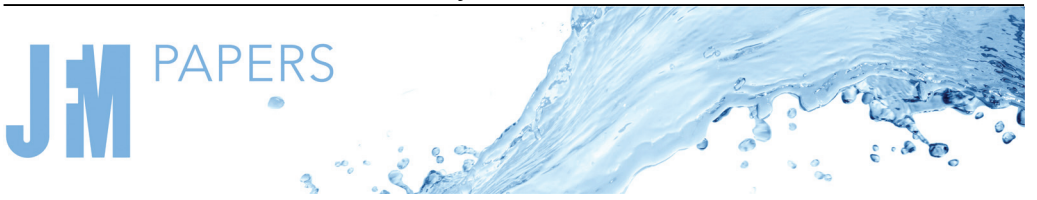

Modelling the passive breakup of a surfactant-contaminated droplet in a T-junction microchannel

Jinggang Zhang[1],†, **Yongguang Wang**[1], **Li Chen**[1], **Linjun Shen**[1] and **Haihang Cui**[1],†

[1]School of Building Services Science and Engineering, Xi'an University of Architecture and Technology, Xi'an 710055, China

(Received 2 November 2023; revised 20 March 2024; accepted 29 March 2024)

A lattice Boltzmann method is used to explore the effect of surfactants on the unequal volume breakup of a droplet in a T-junction microchannel, and the asymmetry due to fabrication defects in real-life microchannels is modelled as the pressure difference between the two branch outlets (ΔP^*). We first study the effect of the surfactants on the droplet dynamics at different dimensionless initial droplet lengths (l_0^*) and capillary numbers (Ca) under symmetric boundary conditions ($\Delta P^* = 0$). The results indicate that the presence of surfactants promotes droplet deformation and breakup at small and moderate l_0^* values, while the surfactant effect is weakened at large l_0^* values. When the branch channels are completely blocked by the droplet, a linear relationship is observed between the dimensionless droplet length (l_d^*) and dimensionless time (t^*), and two formulas are proposed for predicting the evolution of l_d^* with t^* for the two systems. We then investigate the effect of the surfactants on the droplet breakup at different values of ΔP^* and bulk surfactant concentrations (ψ_b) under asymmetric boundary conditions ($\Delta P^* \neq 0$). It is observed that, as ΔP^* increases, the volume ratio of the generated droplets (V_1/V_2) decreases to 0 in both systems, while the rate of decrease is higher in the clean system, i.e. the presence of surfactants could cause a decreased pressure difference between the droplet tips. As ψ_b increases, V_1/V_2 first increases rapidly, then remains almost constant and finally decreases slightly. We thus establish a phase diagram that describes the V_1/V_2 variation with ΔP^* and ψ_b.

Key words: drops, liquid bridges, microfluidics

† Email addresses for correspondence: jinggangzhang@stu.xjtu.edu.cn, cuihaihang@xauat.edu.cn

1. Introduction

Droplet-based microfluidic devices are critical in research areas such as bioanalysis (Sharma & Sharma 2022; Xu *et al.* 2022; Sun *et al.* 2023), disease surveillance (Giuffrida, Cigliana & Spoto 2018; Nix *et al.* 2022), the synthesis of nanomaterials (Zou *et al.* 2022; Gimondi *et al.* 2023; Yao *et al.* 2023) and microchemical reactors (Whitesides 2006; Verma & Pandya 2022). In these areas, droplets with controlled volume and good uniformity are prerequisites for ensuring device accuracy and sensitivity. T-junction microchannels have been widely used to passively split droplets into two daughter droplets comprising similar volumes (Leshansky & Pismen 2009). In practical applications, fabrication defects inevitably exist in microchannels, which not only result in asymmetry between the two branch channels, but also generate daughter droplets of different volumes. Although active agents or surfactants are known to promote droplet breakup and prevent droplets from coalescing (Baret *et al.* 2009; Pan *et al.* 2016), their effects on the disturbed flow field, neck contraction process and enhancement or weakening of the disturbances caused by tiny deficiencies and defects are still unclear. Therefore, it is necessary to understand the effect of surfactants on the passive breakup of a droplet in a T-junction microchannel, which is helpful for controlling the surfactant dosage and generating droplets with controlled volume.

Numerous studies have been conducted to investigate the passive break-up of droplets flowing through T-junction microchannels. Hoang *et al.* (2013) numerically studied the breakup of three-dimensional droplets under the action of creeping flow in symmetric T-junction microchannels. They found that the droplet breakup process can be divided into two stages: (I) the droplet deforms under the action of an external flow field, and (II) the droplet neck rapidly contracts and breaks up owing to the Reyleigh–Plateau instability (Rayleigh 1878). They also reported that the droplet neck begins to spontaneously pinch off when the neck curvature is higher than the curvature of the rest of the interface and that the breakup mechanism is similar to the end-pinching mechanism for unconfined droplets proposed by Stone, Bentley & Leal (1986). Chen & Deng (2017) used the phase-field lattice Boltzmann (LB) model to study the dynamic behaviour of droplets flowing through T-shaped microchannels. They found that the appearance of a tunnel (the tunnel between the droplet and channel sidewalls) was a prerequisite for the final non-breakup of the droplet. The tunnel effect not only slows down the droplet deformation rate, but may also induce non-breakup of the droplet in the T-junction microchannel. Chen, Xue & Hu (2019) numerically studied the droplet breakup process in symmetric microfluidic T-junctions comprising circular tubes. They found that the neck collapsed suddenly when the capillary pressure at the centre of the droplet neck was balanced by the pressure inside the neck. At the same time, the average radius of the neck was approximately 0.51 times the channel radius.

The size of the microchannel is usually at the micron level (Hoang *et al.* 2014); therefore, any minor disturbances, such as fluctuations in the inlet flow rate and outlet pressure, and the non-uniformity of the wall roughness, will have an impact on the breakup behaviour of droplets in T-junction microchannels. Chen & Deng (2017) adopted a phase-field multiphase LB model to study the dynamic behaviour of a two-dimensional droplet flowing through a T-junction microchannel, wherein the interfacial tension along the radial direction of the droplet neck was not considered. When a small pressure fluctuation is applied to the one-branch outlet, the droplet that remains stable at the T-junction begins to undergo asymmetric deformation and eventually drains from the one-branch channel. Hoang *et al.* (2014) experimentally investigated the repeated breakup of bubbles in sequential T-junction microchannels. They stated that the microchannel used in the

experiment is bound to have a small asymmetry owing to the limitations of the current microchannel process technology, which is one of the reasons why the droplet breaks up into sub-droplets of different volumes. Samie, Salari & Shafii (2013) experimentally studied the breakup behaviour of a droplet in an asymmetric T-junction microchannel with two branches of identical lengths and different cross-sections. As the cross-sectional area ratio of the two branch channels increases, the breakup model of the mother droplet first changes from a symmetric breakup to an asymmetric breakup, and finally to a non-breakup, and the droplet drains from one branch channel. Fu, Ma & Li (2014) experimentally investigated the breakup process of bubbles in T-shaped microchannels, where the lengths of the two branch channels were unequal. They found that the difference in volume between the sub-bubbles first exhibited an increasing and then decreasing trend as the injection ratio of the continuous fluid was increased.

Considerable research has thus been conducted to elucidate the passive breakup mechanisms of clean droplets in T-junction microchannels. However, little attention has been focused on the effect of surfactants on the breakup mechanism. The characteristic size of the T-junction microchannels is usually in the micron level, so the tiny deficiencies and defects in microchannels can seriously affect the flow field and thus generate daughter droplets of different volumes. To the best of our knowledge, little research has focused on how to suppress such small perturbations to generate daughter droplets of equal volumes. In addition, the experiments failed to accurately measure the volume of the generated droplets and neck thickness, and to capture the distributions of the velocity magnitude and surfactant concentration (Zhu & Wang 2017). Comparatively speaking, numerical simulations can not only overcome the aforementioned shortcomings, but also facilitate the individual adjustment of the influencing parameters to arrive at universal laws.

In this paper, we adopt our recently developed LB method (Zhang *et al.* 2023*a*) to study the effect of the surfactants on a droplet flowing through a T-junction microchannel. We first investigate the effect of surfactants on the droplet dynamics under a symmetric boundary condition ($\Delta P^* = 0$). The surfactant role is identified by comparing the droplet morphology, neck contraction process, neck breakup time and flow pattern between the clean and surfactant-contaminated systems under different values of the initial droplet length and capillary number. A pressure difference is then introduced between the two branch outlets in the multiphase systems to represent the small disturbance. Under the action of the pressure difference ($\Delta P^* \neq 0$), the mother droplet may break up asymmetrically or flow into one branch channel. The effects of the surfactants on the asymmetric breakup of the mother droplet are identified by comparing the volume ratio of the two generated droplets (V_1/V_2) between the two systems under different values of ΔP^* and bulk surfactant concentration (ψ_b). Finally, a phase diagram that describes how V_1/V_2 varies with ΔP^* and ψ_b is presented.

2. Problem statement

We consider the passive breakup of a surfactant-contaminated droplet in a T-junction microchannel (figure 1), where green and grey indicate the droplet interface and channel wall, respectively. The microchannel is composed of a vertical entrance channel of length $L_1 = 150$ μm, width $W = 30$ μm and height $H = 30$ μm and two horizontal branch channels of the same width and height. The length of the horizontal channel is $L = 200$ μm, and the vertical channel is located in the middle of the horizontal channel. The densities of the continuous and dispersed fluids are $\rho^R = \rho^B = 1000$ kg m^{-3}; the dynamic viscosities of the continuous and dispersed fluids are $\mu^R = 8\mu^B = 0.008$ Pa s; the interfacial tension is $\sigma = 0.005$ N m. A constant inlet velocity u_{in} is imposed at the

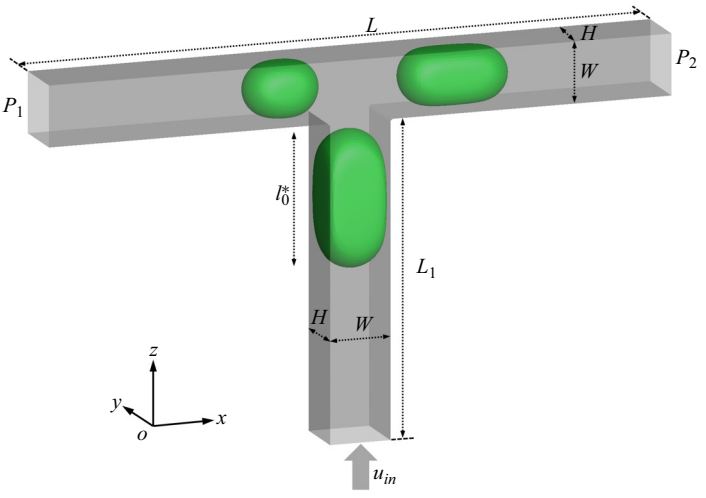

Figure 1. Diagram of the surfactant-contaminated droplet breakup in a T-junction microchannel, where the droplet interface and microchannel wall are indicated in green and grey, respectively. The constant velocity u_{in} is imposed at the bottom inlet, while the constant pressures P_1 and P_2 are respectively imposed at the left and right branch outlets, respectively.

inlet, and two constant pressures (P_1 and P_2) are imposed at the left and right branch outlets, respectively. Driven by the injected fluid, a droplet of initial dimensionless length l_0^* flows from the vertical channel into the T-junction with two branches of equal length.

To obtain the LB simulation parameters, three reference quantities are selected, i.e. the time scale $T_0 = 10^{-7}$ s, length scale $L_0 = 10^{-6}$ m and mass scale $M_0 = 10^{-15}$ kg. A physical parameter having the dimensions $(\mathrm{m})^{n1}(\mathrm{s})^{n2}(\mathrm{kg})^{n3}$ is divided by $(L_0)^{n1}(T_0)^{n2}(M_0)^{n3}$ to obtain the value of the corresponding LB parameter. Following this criterion, we can obtain the LB simulation parameters: $W_{LB} = W/L_0 = 30$, $\rho_{LB}^R = \rho_{LB}^B = \rho^R/(M_0/L_0^3) = 1$, $\mu_{LB}^R = 8\mu_{LB}^B = \mu^R/(M_0/L_0T_0) = 0.8$ and $\sigma_{LB} = \sigma_0/(M_0/T_0^2) = 0.005$, where the subscript '$LB$' indicates the LB parameter and is used to distinguish between the LB and physical parameters. Unless stated otherwise, the pressures imposed at the left and right branch outlets are considered as $P_1 = P_2 = P_0 = \rho_0 c_s^2 = 1/3$, where $\rho_0 = 1$ is the initial density of the two fluids, and $c_s = 1/\sqrt{3}$ is the speed of sound (Hafen *et al.* 2023). The static contact angle is fixed at $\theta_0 = 0^\circ$, indicating that the microchannel wall completely halts the dispersed fluid. For the surfactant-contaminated system, the bulk surfactant concentration is considered to be $\psi_b = 0.1$, and the elasticity number is considered as $E_0 = 0.5$. The mobility is fixed at $M_\psi = 0.01$, and the diffusivity and bulk surfactant solubility are considered to be $Pi = 1.35$ and $E_x = 0.117$ (Soligo, Roccon & Soldati 2019, 2020), respectively.

The problem is characterized using four dimensionless parameters, i.e. the capillary number Ca, Reynolds number Re, dimensionless pressure difference ΔP^* and viscosity ratio λ, which are given by

$$Ca = \frac{\mu^R u_{in}}{\sigma_0}, \quad Re = \frac{\rho^R W u_{in}}{\mu^R}, \quad \Delta P^* = P_1^* - P_2^*, \quad \lambda = \frac{\mu^R}{\mu^B}, \tag{2.1a–d}$$

where the dimensionless pressures P_1^* and P_2^* are denoted as $P_1^* = P_1/P_0$ and $P_2^* = P_2/P_0$, respectively; $\Delta P^* = 0$ and $\Delta P^* \neq 0$ represent the symmetric and asymmetric boundary conditions, respectively. For the flow regimes under consideration, the Reynolds number

is small ($0.012 \leq Re \leq 0.070$); therefore, the inertial effect can be neglected compared with the viscous effect. The viscosity ratio is fixed at $\lambda = 8$ to reduce the influencing parameters. Therefore, two dimensionless parameters (Ca and ΔP^*) are left to characterize the problem.

As in the experiments (Chagot *et al.* 2022; Kalli & Angeli 2022) and numerical simulations (Zhang *et al.* 2022, 2023*a*), the breakup process of a droplet in a T-junction for clean and surfactant-contaminated systems is compared for the same dimensionless parameters, which indicates that the differences between the two systems can be attributed to the reduced interfacial tension caused by the adsorption of surfactants at the droplet interface and the Marangoni stress caused by the non-uniform distribution of surfactants at the droplet interface.

3. Numerical method

In this study, our recently developed LB method (Zhang *et al.* 2023*a*) is used to simulate the hydrodynamics of surfactant-contaminated droplets in a T-junction microchannel. In this method, a colour-gradient model is used to solve the two-phase flows, and an additional LB model is used to solve the surfactant transport. These two models are coupled using a modified Langmuir equation of state (Liu *et al.* 2020; Zhang *et al.* 2021*a*), which allows the surfactant concentration to reach or exceed the critical micelle concentration (CMC). Furthermore, a 'predictor–corrector' wetting boundary condition (Xu, Liu & Valocchi 2017; Akai, Bijeljic & Blunt 2018; Zhang *et al.* 2023*a*,*b*) is adopted to enforce the contact angle on an arbitrary solid surface. A compact summary of this method is provided below.

3.1. *The LB colour-gradient model for immiscible two-phase flows*

In the LB colour-gradient model, f_i^B and f_i^R denote blue and red fluids, respectively, and the subscript i represents the ith lattice velocity direction. The total distribution function is defined as $f_i = f_i^B + f_i^R$. First, the collision step is executed for f_i, which reads as follows (Jiang *et al.* 2021):

$$f_i^{\dagger}(\boldsymbol{x}, t) = f_i(\boldsymbol{x}, t) + \Omega_i(\boldsymbol{x}, t) + \bar{F}_i, \tag{3.1}$$

where $f_i(\boldsymbol{x}, t)$ and $f_i^{\dagger}(\boldsymbol{x}, t)$ are the pre- and post-collision distribution functions in the ith lattice velocity direction at the spatial coordinates $\boldsymbol{x}$ and time t and $\bar{F}_i$ is the forcing term. The parameter $\Omega_i(\boldsymbol{x}, t)$ is the multiple-relaxation-time collision operator, which is expressed as follows (Zhang, Liu & Ba 2019):

$$\Omega_i(\boldsymbol{x}, t) = -\sum_j (\boldsymbol{M}^{-1}\boldsymbol{S}\boldsymbol{M})_{ij}(f_j(\boldsymbol{x}, t) - f_j^{eq}(\boldsymbol{x}, t)), \tag{3.2}$$

where $\boldsymbol{S}$ is the diagonal relaxation matrix and $\boldsymbol{M}$ is the transformation matrix, which can be obtained from the study of Wang, Liu & Zhang (2016); f_i^{eq} is the equilibrium distribution function as defined by Wei *et al.* (2018)

$$f_i^{eq} = \rho w_i \left[1 + \frac{\boldsymbol{e}_i \cdot \boldsymbol{u}}{c_s^2} + \frac{(\boldsymbol{e}_i \cdot \boldsymbol{u})^2}{2c_s^4} - \frac{\boldsymbol{u}^2}{2c_s^2}\right], \tag{3.3}$$

where $\boldsymbol{u}$ is the fluid velocity and $\rho = \rho^B + \rho^R$ is the total density, where ρ^B and ρ^R are the densities of the blue and red fluids, respectively. The speed of sound c_s, weighting factors w_i and lattice velocities $\boldsymbol{e}_i$ can be obtained from the study of Wang *et al.* (2016).

The expression for $\boldsymbol{S}$ in (3.2) is given by Liu *et al.* (2020) as follows:

$$\boldsymbol{S} = \mathrm{diag}[0, s_1, s_2, 0, s_4, 0, s_4, 0, s_4, s_9, s_{10}, s_9, s_{10}, s_{13}, s_{13}, s_{13}, s_{16}, s_{16}, s_{16}], \tag{3.4}$$

with

$$s_1 = s_2 = s_9 = s_{10} = s_{13} = \omega, \quad s_4 = s_{16} = 8(2 - s_1)/(8 - s_1), \tag{3.5a,b}$$

where the parameter ω is related to the dynamic viscosity μ as $\mu = (1/\omega - 0.5)\rho c_s^2 \delta_t$. A harmonic function is used to ensure the smooth transition of the viscosity across a two-phase interface comprising unmatched viscosities, and it is given by

$$\frac{1}{\mu} = \frac{1 - \rho^N}{2\mu^B} + \frac{1 + \rho^N}{2\mu^R}, \tag{3.6}$$

where μ^B and μ^R are the dynamic viscosities of the blue and red fluids, respectively. The index function ρ^N is responsible for identifying the position of the fluid–fluid interface, which is defined as $\rho^N = (\rho^R - \rho^B)/(\rho^R + \rho^B)$.

The interfacial force $\bar{F}_i$ in (3.1) is defined as follows (Yu & Fan 2010):

$$\bar{F}_i = \sum_j \left(\boldsymbol{I} - \frac{1}{2}\boldsymbol{M}^{-1}\boldsymbol{S}\boldsymbol{M} \right)_{ij} w_j \left[\frac{\boldsymbol{e}_j - \boldsymbol{u}}{c_s^2} + \frac{(\boldsymbol{e}_j \cdot \boldsymbol{u})\boldsymbol{e}_j}{c_s^4} \right] \cdot \boldsymbol{F}_s \delta_t, \tag{3.7}$$

where $\boldsymbol{I}$ is the 9×9 unit matrix. The interfacial force $\boldsymbol{F}_s$ consists of the interfacial tension force and Marangoni stress due to the non-uniform interfacial tension, which is given as (Zhang *et al.* 2021*a*)

$$\boldsymbol{F}_s = -\tfrac{1}{2}\sigma k \nabla \rho^N + \tfrac{1}{2}|\nabla \rho^N| \nabla_s \sigma, \tag{3.8}$$

where σ is the interfacial tension. The interface curvature k is defined as $k = -\nabla_s \cdot \boldsymbol{n} = -[\nabla - \boldsymbol{n}(\boldsymbol{n} \cdot \nabla)] \cdot \boldsymbol{n}$, where the unit normal vector of the fluid–fluid interface $\boldsymbol{n}$ is defined as $\boldsymbol{n} = -\nabla \rho^N / |\nabla \rho^N|$. The first and second terms on the right side of (3.8) are the interfacial tension force and Marangoni stress, respectively.

Following a previous study (Zhang, Liu & Zhang 2021*b*), a modified Langmuir equation of state is adopted to describe the variation in the interfacial tension $\sigma(\psi)$ with the surfactant concentration, which is given by

$$\sigma(\psi) = \max\{\sigma_{min},\ \sigma_0[1 + E_0 \log(1 - \psi)]\}, \tag{3.9}$$

where E_0 is the elasticity number, ψ is the dimensionless surfactant concentration, σ_0 is the interfacial tension in the absence of surfactants and σ_{min} is the minimum interfacial tension, which is set as $\sigma_0/3$ to avoid obtaining non-physical negative values for $\sigma(\psi)$.

Subsequently, a recolouring step is implemented to separate the two immiscible fluids and maintain a reasonably diffuse interface. Finally, the propagation step is executed to transport f_i^B and f_i^R to adjacent lattice nodes. These two steps are identical to those adopted by Zhang *et al.* (2019). The distribution function after the streaming step is used to calculate the densities and velocities of the two fluids, i.e. $\rho^k(\boldsymbol{x}, t) = \sum_i f_i^k(\boldsymbol{x}, t)$ and $\rho \boldsymbol{u}(\boldsymbol{x}, t) = \sum_i f_i^k(\boldsymbol{x}, t)\boldsymbol{e}_i + 0.5 \cdot \boldsymbol{F}_s(\boldsymbol{x}, t)\delta_t$, where $k =$ or R.

3.2. *The LB model for surfactant transport*

The transportation of soluble surfactants is described by the Cahn–Hilliard equation given by Soligo *et al.* (2019) and Zong *et al.* (2020)

$$\frac{\partial \psi}{\partial t} + \boldsymbol{u} \cdot \nabla \psi = \frac{1}{Pe} \nabla \cdot (M_\psi \nabla \mu_\psi), \tag{3.10}$$

where the mobility M_ψ is taken as 0.01 and the Péclet number Pe is taken as 10 (Zhang *et al.* 2023*a*). The chemical potential μ_ψ is expressed as

$$\mu_\psi = Pi \log\left(\frac{\psi}{1-\psi}\right) - \frac{[1-(\rho^N)^2]^2}{4} + \frac{(\rho^N)^2}{2E_x}, \tag{3.11}$$

where the parameters E_x and Pi are used to control the bulk surfactant solubility and surfactant diffusivity, respectively.

The LB method is used to solve (3.10), which is written as (Liang *et al.* 2014; Zhang *et al.* 2021*a*)

$$\begin{aligned} &g_i(\boldsymbol{x} + \boldsymbol{e}_i \delta_t,\ t + \delta_t) - g_i(\boldsymbol{x},\ t) \\ &\quad = -\frac{1}{\tau_g}[g_i(\boldsymbol{x},\ t) - g_i^{eq}(\boldsymbol{x},\ t)] + w_i \frac{\boldsymbol{e}_i \cdot \boldsymbol{u}}{c_s^2} \partial_t \psi \delta t, \end{aligned} \tag{3.12}$$

where g_i is the distribution function of ψ. The dimensionless relaxation time τ_g is set as 1 (Wang *et al.* 2016). Here, g_i^{eq} is the equilibrium distribution function of g_i, which is written as (Wang *et al.* 2016)

$$g_i^{eq} = w_i(G_i + 3\psi \boldsymbol{e}_i \cdot \boldsymbol{u}), \tag{3.13}$$

with

$$G_i = \begin{cases} [\psi - (1-w_0)\Gamma\psi/c_s^2]/w_0, & i = 0 \\ \Gamma\psi/c_s^2, & i > 0 \end{cases}, \tag{3.14}$$

where the parameter Γ is connected to M_ψ by $M_\psi = \delta_t \Gamma(\tau_g - 0.5)$.

Wang *et al.* (2016) proved that (3.12) can be rewritten as shown in (3.10) within the limitation of a low Mach number using the Chapman–Enskog analysis. The surfactant concentration ψ is calculated using $\psi(\boldsymbol{x}, t) = \sum_i g_i(\boldsymbol{x}, t)$.

3.3. *Wetting boundary conditions*

The contact angle formed between the solid substrate and the fluid–fluid interface is used to quantify the solid wettability. In this study, we assume that the presence of surfactants only decreases the fluid–fluid interfacial tension, but does not affect the solid–fluid interfacial tension. Therefore, the relationship between the dynamic contact angle $\theta(\psi)$ and the surfactant concentration can be obtained as follows (Zhang *et al.* 2021*a*):

$$\theta(\psi) = \arccos\left(\frac{\cos\theta_0}{1 + E_0 \log(1-\psi)}\right), \tag{3.15}$$

where θ_0 is the static contact angle in the absence of surfactants.

Subsequently, the 'predictor–corrector' wetting boundary condition is used to enforce the dynamic contact angle $\theta(\psi)$ on an arbitrary solid surface. The basic concept of this boundary condition is to modify the orientation of the index function gradient $\nabla \rho^N$ to

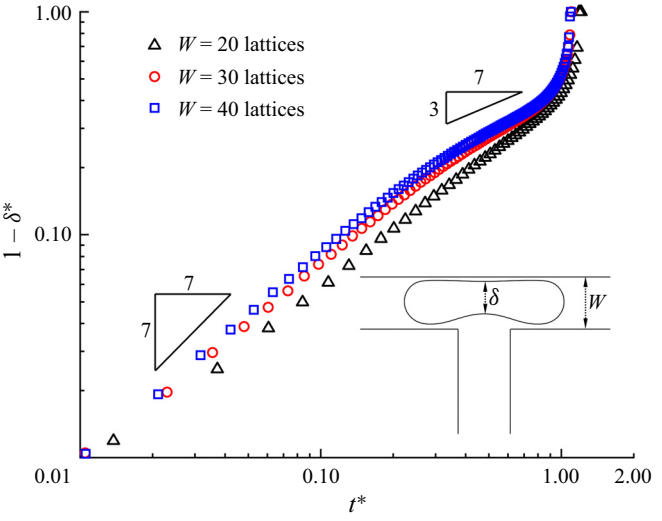

Figure 2. Time evolution of dimensionless neck thickness δ^* at three different grid resolutions for clean system ($\psi_b = 0$). The dimensionless neck thickness and time are defined as $\delta^* = \delta/W$ and $t^* = Ca\,\sigma_0 t/\mu^R W$, respectively. The black triangles, red circles and blue squares correspond to the mesh sizes of $W = 20$, 30 and 40 lattices, respectively. The other parameters are fixed at $Ca = 0.01$, $l_0^* = 3.5$ and $\Delta P^* = 0$.

achieve the desired contact angle. Details of the implementation steps can be found in previous studies (Xu *et al.* 2017; Akai *et al.* 2018; Zhang *et al.* 2023*a*,*b*).

It should be noted that our numerical method has been validated against the experimental results by simulating the generation of clean droplets in T-junction microchannels (Zhang *et al.* 2022) as well as the analytical solutions for the invasion velocity and minimum pressure difference of a clean droplet invading a capillary tube with variable cross-sections (Zhang *et al.* 2023*a*). In addition, our method was validated by comparing the numerical results of the equilibrium surfactant distribution across a two-phase interface with the analytical profile in both two- and three-dimensional cases (Zhang *et al.* 2021*a*, 2023*a*).

4. Grid independence test and validation

Before further validating our numerical method, a grid-independence test was conducted to determine a reasonable grid resolution. Figure 2 presents the dimensionless neck thickness δ^* as a function of the dimensionless time t^* for a clean droplet breakup in a T-junction microchannel, where the black triangles, red circles and blue squares correspond to three different mesh sizes ($W = 20$, 30 and 40 lattices). Each mesh size corresponds to the physical channel width of 30 μm. The dimensionless time is defined as $t^* = Ca\,\sigma_0 t/\mu^R W$, and the time for the droplet to completely enter the horizontal channel is considered to be $t^* = 0$. The dimensionless neck thickness δ^* is defined as $\delta^* = \delta/W$, where δ is the droplet neck thickness (inset image). It can be observed from the figure that the numerical results gradually converge as W increases. In particular, the numerical results for $W = 30$ lattices and 40 lattices are coincident, indicating that the grid resolution is sufficiently high for the two grid resolutions.

The breakup process of a droplet in a T-junction microchannel can be divided into two stages based on the exponent of the scaling law (Leshansky *et al.* 2012). In the first stage, $1 - \delta^*$ has a linear relationship with t^*. However, in the subsequent stage, $1 - \delta^* \sim t^{*3/7}$

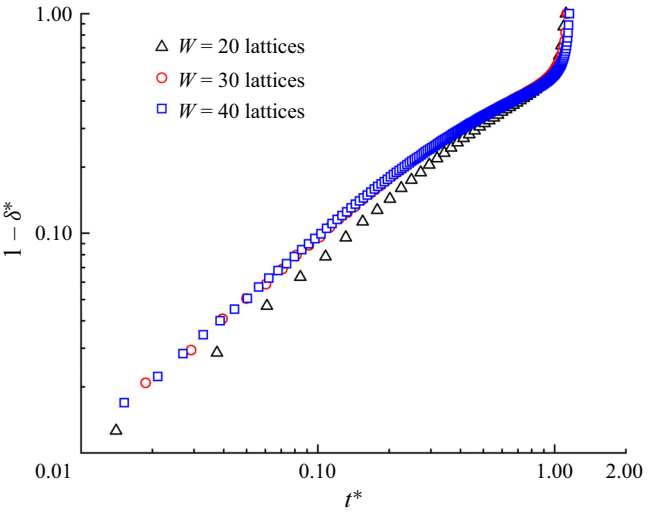

Figure 3. Time evolution of dimensionless neck thickness δ^* at three grid resolutions for a surfactant-contaminated system ($\psi_b = 0.1$). The black triangles, red circles and blue squares correspond to the mesh sizes of $W = 20$, 30 and 40 lattices, respectively. The other parameters are fixed at $Ca = 0.01$, $l_0^* = 3.5$ and $\Delta P^* = 0$.

causes the droplet neck to collapse rapidly within a finite time. This scaling law exponent has been widely validated by Leshansky *et al.* (2012), Hoang *et al.* (2013), Chen & Deng (2017) and Wang *et al.* (2015). As shown in figure 2, the time evolution of $1 - \delta^*$ can be described by the analytical scaling 1 law in the former stage and by the analytical 3/7 scaling law in the subsequent stage. This indicates that our proposed numerical method could capture the transient breakup process of the droplet.

Because our recent work (Zhang *et al.* 2023*a*) has shown that our numerical method can correctly describe surfactant transport in a bulk solution and at the fluid–fluid interface, only a grid independence test is required to select a reasonable grid resolution. Figure 3 presents the temporal evolution of the dimensionless neck thickness δ^* for the surfactant-contaminated system ($\psi_b = 0.1$), where three mesh sizes ($W = 20$, 30 and 40 lattices) are presented. It can be observed that the numerical results are independent of the channel width when $W \geq 30$ lattices, which is the same as the case of the clean system (figure 2). To balance the computational requirements and model performance, the channel width of the $W = 30$ lattices is selected for both the clean and surfactant-contaminated systems in the following simulations.

5. Results and discussion

In this section, we study the passive breakup process of droplets in T-junction microchannels under symmetric and asymmetric boundary conditions, i.e. $\Delta P^* = 0$ and $\Delta P^* \neq 0$. These two boundary conditions are realized by reducing the right branch outlet pressure (P_2^*), while maintaining the left branch outlet pressure (P_1^*) at a constant. The effect of surfactants on the droplet breakup process under two boundary conditions is identified by comparing clean and surfactant-contaminated systems with the same dimensionless parameters.

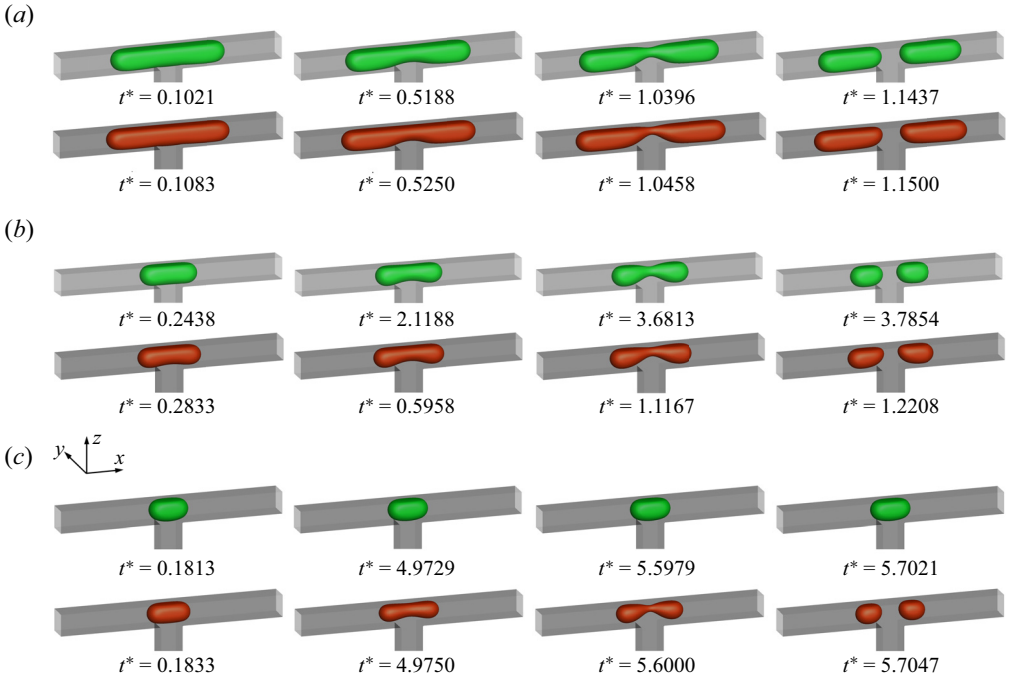

Figure 4. Temporal evolution of the droplet interface ($\rho^N = 0$) at (*a*) $l_0^* = 3.5$, (*b*) $l_0^* = 1.5$ and (*c*) $l_0^* = 1$ for the clean (top row) and surfactant-contaminated systems (bottom row), where the dimensionless time is defined as $t^* = Ca\,\sigma_0 t/(\mu^R W)$. The clean droplet interface, surfactant-contaminated droplet interface and microchannel wall are indicated green, red and grey, respectively. The other parameters are fixed at $Ca = 0.01$, $\psi_b = 0.1$ and $\Delta P^* = 0$.

5.1. *Symmetric boundary condition*

This subsection presents an examination of the effect of surfactants on the droplet breakup process in a T-junction microchannel under symmetric boundary conditions ($\Delta P^* = 0$), where the surfactant role is identified by comparing the droplet morphology, temporal evolution of the droplet neck thickness and breakup time at the same dimensionless initial droplet length l_0^* and capillary number Ca.

5.1.1. *Effect of initial droplet length*

The effect of the dimensionless initial droplet length l_0^* on the droplet breakup process is investigated by decreasing l_0^* from 3.5 to 0.75. Figure 4 displays the temporal evolution of the droplet interface ($\rho^N = 0$) at (*a*) $l_0^* = 3.5$, (*b*) $l_0^* = 1.5$ and (*c*) $l_0^* = 1$ for the clean (top row) and surfactant-contaminated systems (bottom row), where the green, red and grey colours indicate the clean droplet interface, surfactant-contaminated droplet interface and microchannel wall, respectively. It should be noted that the capillary number and bulk surfactant concentration are fixed at $Ca = 0.01$ and $\psi_b = 0.1$, respectively. At $l_0^* = 3.5$ (figure 4*a*), the droplet almost completely blocks the two branch channels in both clean and surfactant-contaminated systems. It can be observed that the shapes of the clean and surfactant-contaminated droplets are nearly identical at the approaching time, and the breakup times of the droplet neck are close. We also observe that the droplet length appears larger in the surfactant-contaminated system than that in the clean system. When l_0^* decreases to 1.5 (figure 4*b*), the surfactant-contaminated droplet deforms

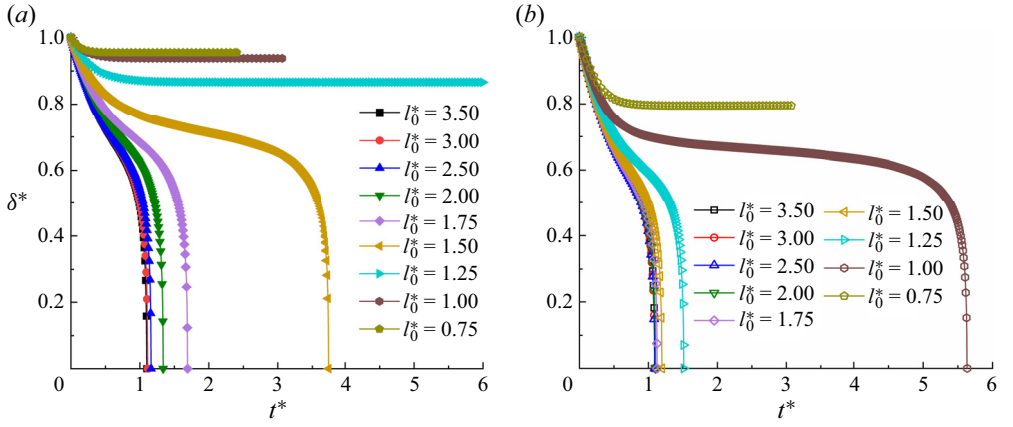

Figure 5. Time evolution of the dimensionless neck thickness δ^* under different values of the dimensionless initial droplet length l_0^* for (*a*) the clean system and (*b*) surfactant-contaminated system, where δ^* is defined as $\delta^* = \delta/W$.

faster than the clean droplet, and the breakup time of the droplet neck is shorter in the surfactant-contaminated system than that in the clean system. As in the case of $l_0^* = 3.5$, the length of the surfactant-contaminated droplet also appears to be larger than that of the clean droplet. Upon further decreasing l_0^* to 1 (figure 4*c*), the clean droplet eventually maintains a steady-state shape and stays at the T-junction, while the surfactant-contaminated droplet continues to deform over time and eventually breaks up into two daughter droplets of similar volumes. These phenomena suggest that the effect of the surfactants on the droplet dynamics is relatively weak at larger l_0^* values (a comparison between the top and bottom rows is presented in figure 4*a*), while the surfactant effects are conducive to the droplet deformation and breakup at moderate and smaller l_0^* values (a comparison between the top and bottom rows is presented in figure 4*b*,*c*).

A quantitative evolution of the dimensionless neck thickness δ^* with the dimensionless time t^* for both clean and surfactant-contaminated systems is presented in figures 5(*a*) and 5(*b*), respectively. It should be noted that δ^* is defined as $\delta^* = \delta/W$. In the cases of the droplet breakup, i.e. when δ^* eventually decreases to zero, the breakup process can be divided into two stages. In the former stage, δ^* slowly decreases as t^* increases. In this stage, the inertial force dominates the neck contraction process, and the injected fluid compresses the droplet interface and reduces the thickness of the droplet neck. Meanwhile, the deformation of the droplet interface alleviates the compression of the injected fluid on the droplet neck, resulting in a decrease in the neck contraction rate. In the subsequent stage, the interfacial tension dominates the neck contraction process, and δ^* rapidly decreases to zero within a finite time owing to the Rayleigh–Plateau instability (Plateau 1873; Rayleigh 1878). In addition, we also notice some differences in the droplet non-breakup cases between the two systems. It can be observed from the figure that δ^* first decreases and then maintains a non-zero value as t^* increases when $l_0^* \leq 1.25$ for the clean system (figure 5*a*), while a similar evolution of δ^* occurs with t^* when $l_0^* = 0.75$ for the surfactant-contaminated system (figure 5*b*). This means that the presence of surfactants promotes the breakup of the droplet. We also note that the curve of δ^* varying with t^* overlaps when $l_0^* \geq 2.5$ for the clean system (figure 5*a*), while it overlaps when $l_0^* \geq 1.5$ for the surfactant-contaminated system (figure 5*b*). At large values of l_0 (figure 4*a* presents an example), the continuous fluid can no longer flow through the tunnel between the droplet interface and channel wall, which compresses the droplet neck and causes the neck

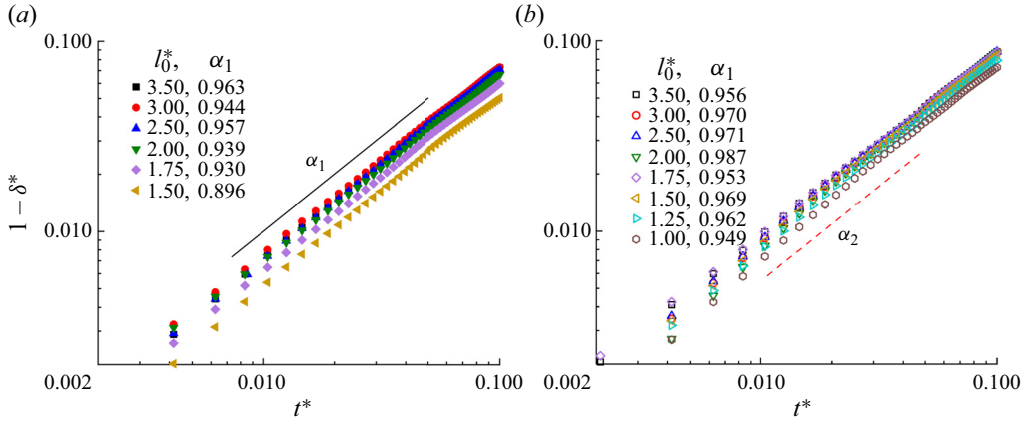

Figure 6. Evolution of the neck thickness for various initial droplet lengths for the (*a*) clean and (*b*) surfactant-contaminated systems.

to contract. At small values of l_0, however, the channel is partially blocked by the droplet (bottom row of figure 4*c*). The injected fluid not only squeezes the droplet to form a neck, but also flows through the tunnel between the droplet interface and channel wall. Therefore, the rate of decrease of δ^* with t^* depends not only on the injection rate of the continuous fluid, but also on the width of the tunnel between the droplet interface and channel wall. In order to explain the difference in the time evolution of δ^* between the two systems, it is necessary to quantify the degree of blockage of the droplet to the branch channels.

Figure 6 presents the temporal evolution of the dimensionless neck thickness δ^* versus the dimensionless time t^* for (*a*) the clean and (*b*) surfactant-contaminated systems. In both systems, $1-\delta^*$ has a linear relationship with the dimensionless time t^*, and the parameters α_1 and α_2 are close to 1 in the former stage. In this stage, the effect of the interfacial tension on the droplet dynamics is small owing to little deformation in the droplet rears. The inertia dominates the neck contraction process, and the rear interface keeps moving with the original velocity with little resistance from the interfacial tension. Therefore, a linear relationship between $1-\delta^*$ and t^* is obtained.

When the branch channels are completely blocked by the droplet, i.e. the flow between the droplet interface and channel wall is entirely suppressed, the increase in the droplet length is determined by the injection rate of the continuous fluid. We assume that the tunnels between the droplet tips and microchannel wall remain unchanged during the neck contraction process. The relationships among the initial droplet length l_{in}, droplet length l_d and inlet velocity u_{in} can be established through mass conservation, which is expressed as

$$l_d \cdot \alpha = l_{in} \cdot \alpha + u_{in} \cdot t, \tag{5.1}$$

where α is the ratio of the maximum droplet area to the branch channel area in the y–z plane, and l_d is the length between the left and right droplet tips. By submitting $u_{in} = Ca \cdot \sigma_0/\mu^R$ into (5.1) and dividing W on both sides of the equal sign, we can derive

$$\frac{l_d}{W} = \frac{l_{in}}{W} + \frac{1}{\alpha} \cdot \frac{Ca \cdot \sigma_0}{\mu^R W} \cdot t, \tag{5.2}$$

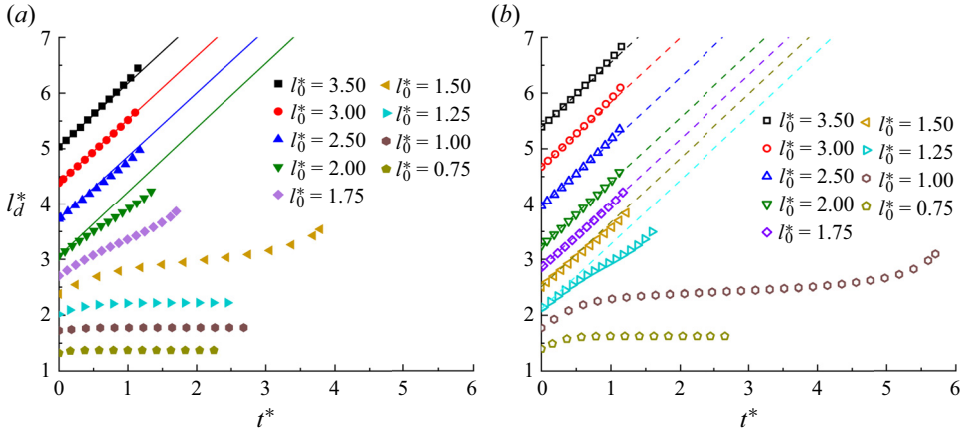

Figure 7. Evolution of the dimensionless droplet length l_d^* with different initial droplet lengths for (*a*) clean and (*b*) surfactant-laden systems, where l_d^* is defined as $l_d^* = l_d/W$. The solid and dashed straight lines are auxiliary lines used to determine whether l_d^* increases linearly with t^*.

which can be simplified as

$$l_d^* = l_{in}^* + \frac{1}{\alpha} \cdot t^*, \tag{5.3}$$

where l_{in}^* is the dimensionless initial droplet length at $t^* = 0$ and l_d^* is the dimensionless droplet length at different values of t^*. This implies that l_d^* increases linearly with t^*, and the corresponding rate of increase is $1/\alpha$.

The temporal evolutions of the dimensionless droplet length l_d^* with different initial droplet lengths for the clean and surfactant-contaminated systems are presented in figures 7(*a*) and 7(*b*), respectively. In this figure, the solid and dashed straight lines are the auxiliary lines used to determine whether l_d^* increases linearly with t^*, and the slopes of the solid and dashed straight lines both are 1.15. In the clean system (figure 7*a*), the variation in l_d^* with t^* is linear when $l_0^* \geq 2.5$, whereas it deviates from the linear relationship when $l_0^* \leq 2$. However, in the surfactant-contaminated system (figure 7*b*), the variation in l_d^* with t^* is linear when $l_0^* \geq 1.5$, whereas it deviates from the linear relationship when $l_0^* \leq 1.25$. The former linear relationship suggests that the corner flow is completely suppressed, i.e. the branch channels are completely blocked by the droplets. Therefore, the evolution of the dimensionless neck thickness δ^* with t^* overlaps when $l_0 \geq 2.5$ and $l_0 \geq 1.5$ for the clean and surfactant-contaminated systems (figure 5), respectively. The latter variation of l_d^* with t^* deviates from the linear relationship because the branch channels are partially blocked by the droplet, and the corner flow alleviates the compression of the injected fluid on the droplet neck. In addition, l_d^* increases linearly with t^* over a wider range of l_0^* in the surfactant-contaminated system than in the clean system. This indicates that the presence of surfactants is conducive to droplet clogging of branch channels. The slopes of the dashed and solid straight lines are identical, suggesting that the rate of increase in $1/\alpha$ depends only on the boundary conditions.

To illustrate the effect of surfactants on the droplet dynamic behaviour when the two branch channels are partially blocked, figure 8 presents a schematic of a surfactant-contaminated droplet flowing through a T-junction under symmetric boundary conditions. Because the branch channels are partially blocked, the injected fluid can flow through the tunnels between the droplet interface and microchannel wall. Under the action of the injected fluid, the surfactants are swept away from the droplet neck and accumulate

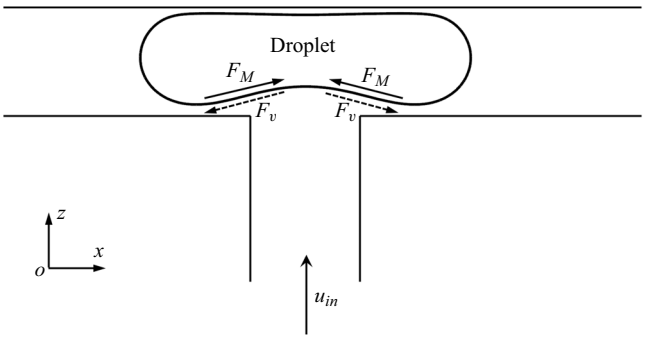

Figure 8. Diagram of surfactant-contaminated droplet passing through T-junction microchannel in x–z middle plane under symmetrical boundary conditions.

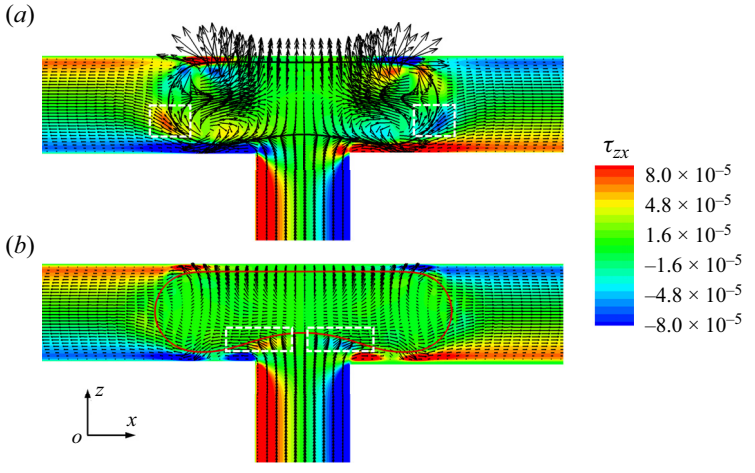

Figure 9. Velocity vectors and the distribution of the shear stress τ_{zx} in the x–z middle plane at $t^* = 1.1167$ for (a) the clean and (b) surfactant-contaminated systems. The black and red curves represent the clean and surfactant-contaminated droplet interfaces, respectively. The other parameters considered are $Ca = 0.01$, $\psi_b = 0.1$, $l_0^* = 1.5$ and $\Delta P^* = 0$.

on both sides of the droplet (right column in figure 11). The uneven distribution of the surfactants at the droplet interface creates two Marangoni stresses F_M, which are directed towards the droplet neck (solid arrows). To balance F_M, two additional viscous drag forces F_v are induced, which are in the direction opposite to that of F_M and act at the droplet interface (dashed arrows). As can be observed, F_v stretches the droplet bottom interface towards the two branch outlets and bottom wall of the branch channels, which is conducive to blocking the branch channels (figure 4b,c). Because the injection rate of the continuous fluid is constant, the enhanced degree of blockage of the droplet to the branch channels causes the continuous fluid to squeeze the droplet neck and reduce the neck thickness, which is helpful for droplet breakup (figures 4b,c and 5). In addition, the presence of surfactants is conducive to the blockage of the droplet in the branch channels, which causes l_d^* to increase linearly with t^* over a wider range of l_0^* (figure 7).

As shown in figure 9, we plot the velocity vectors and distribution of the shear stress τ_{zx} in the x–z middle plane at $t^* = 1.1167$ for (a) the clean and (b) surfactant-contaminated systems. The shear-stress τ_{zx} is given by $\tau_{zx} = \mu(\partial u/\partial z + \partial w/\partial x)$, where u and w are the

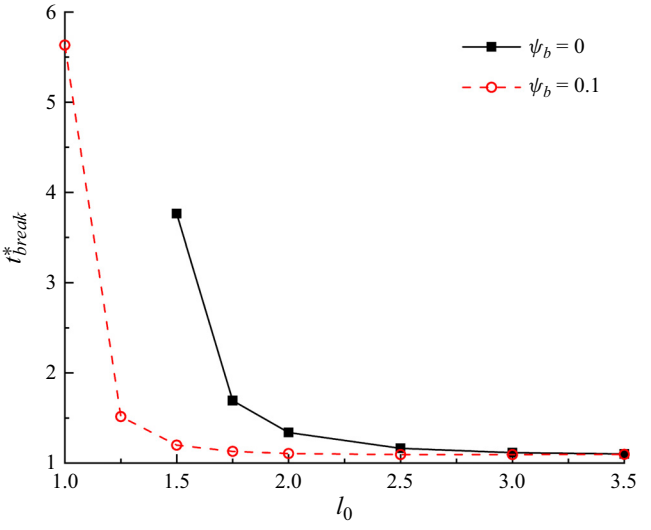

Figure 10. Dimensionless breakup time of the droplet neck (t^*_{break}) as a function of the dimensionless initial droplet length l^*_0 for clean ($\psi_b = 0$) and surfactant-contaminated systems ($\psi_b = 0.1$).

fluid velocities along the x and z directions, respectively. In the clean system (figure 9*a*), the shear stresses are larger on both sides of the droplet interface (indicated by the regions surrounded by white dashed lines), which is conducive to the formation of the vortex inside the droplet. These vortices not only prevent the droplet from stretching, but also prevent the neck from shrinking. However, in the surfactant-contaminated system (figure 9*b*), the shear stresses are large near the lower droplet interface (indicated by the two regions surrounded by white dashed lines), which stretch the droplet bottom interface towards the two branch outlets. This proves that additional viscous drag forces F_v are induced in the surfactant-contaminated system, which stretch the droplet towards the two branch outlets. It can also be observed from the figure that the vortices are formed inside the clean droplet, but no vortex is visible inside the surfactant-contaminated droplet. The direction of the Marangoni stress is opposite to that of the fluid flow; therefore, the interface of the surfactant-contaminated droplet is rigidified (Riaud *et al.* 2018; Zhang *et al.* 2019). Consequently, the vortex formation inside the surfactant-contaminated droplet is suppressed.

Figure 10 presents the variation of the dimensionless breakup time t^*_{break} with the dimensionless initial droplet length l^*_0 for both clean and surfactant-contaminated systems. In either system, t^*_{break} monotonically increases as l^*_0 decreases. As l^*_0 decreases, the blockage caused by the droplet to the branch channels becomes weaker and a part of the continuous fluid flows through the tunnel between the droplet interface and the microchannel wall, thus relieving the compression of the continuous fluid to the droplet neck (Chen & Deng 2017; Sun *et al.* 2019). Therefore, it is more difficult for the droplet neck to form and break up. We also notice that the difference in t^*_{break} between the two systems decreases as l^*_0 increases. At small values of l^*_0, the branch channels are partially blocked, and the corner flow sweeps more surfactants away from the droplet neck, thus resulting in an uneven distribution of surfactants at the droplet interface. As mentioned above, the uneven distribution of surfactants at the droplet interface is conducive to the blockage of the branch channels and the formation of the droplet neck, which promotes the neck breakup. At high values of l^*_0, however, the microchannel is completely blocked

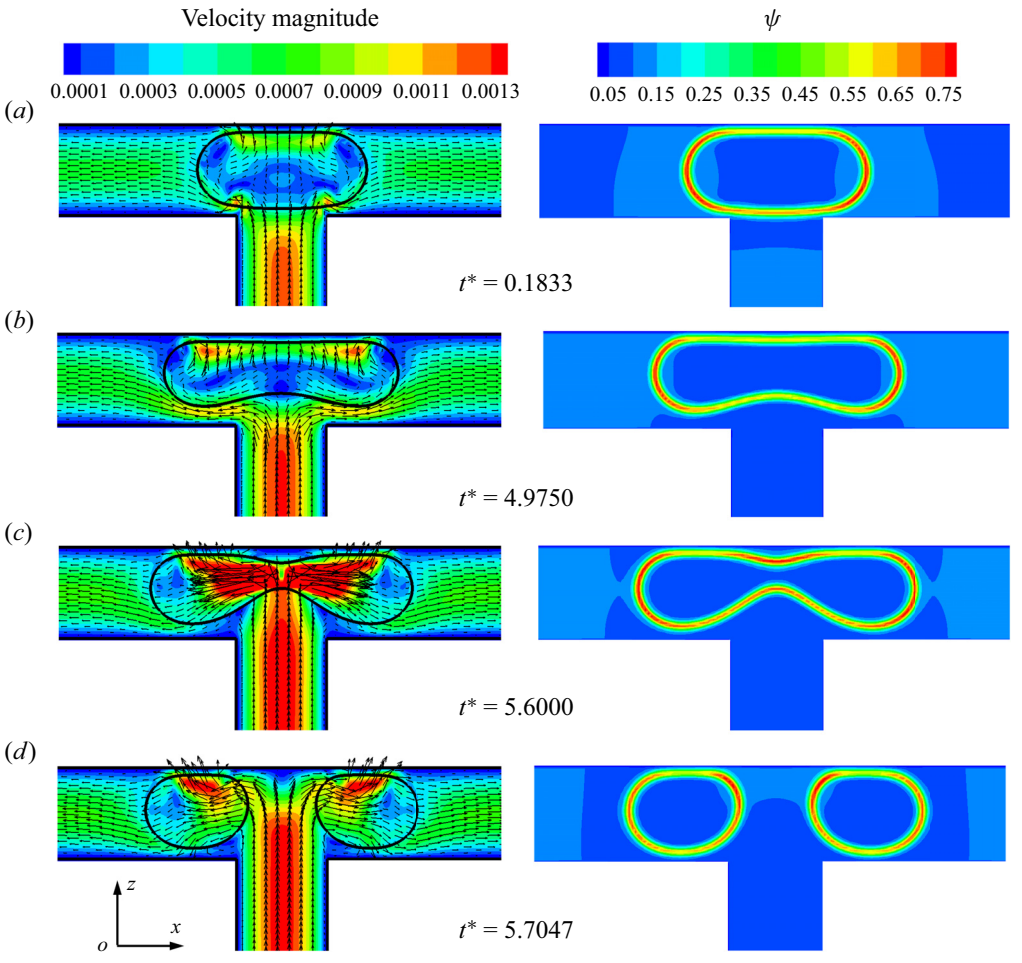

Figure 11. Distributions of the velocity magnitude (left column) and surfactant concentration (right column) in the x–z middle plane for different dimensionless times. The dimensionless initial droplet length is considered as $l_0^* = 1$.

by the droplet, i.e. the corner flow is entirely suppressed, the non-uniform distribution of surfactants at the droplet interface is weakened. The effects of the surfactants on the neck contraction process are accordingly reduced, and the neck contraction process is determined by the injection rate of the continuous fluid.

Figure 11 presents the distributions of the velocity magnitude (left column) and surfactant concentration (right column) in the x–z middle plane for different dimensionless times, where the dimensionless initial droplet length is fixed at $l_0^* = 1$. When the droplet enters the T-junction, the branch channels are blocked by the droplet (at $t^* = 0.1833$). Under the action of the injected fluid, the droplet deforms into a dumbbell shape and the upper interface of the droplet becomes almost parallel to the channel wall (at $t^* = 4.9750$). At the same time, two tunnels between the lower droplet interface and the branch channel wall are symmetrically formed, and two high-velocity regions are formed near both sides of the lower droplet interface. The continuous fluid not only compresses the middle of the droplet to form a neck, but also stretches the droplet towards both sides of the branch channel outlets. As the continuous fluid velocity is directed towards both sides of the

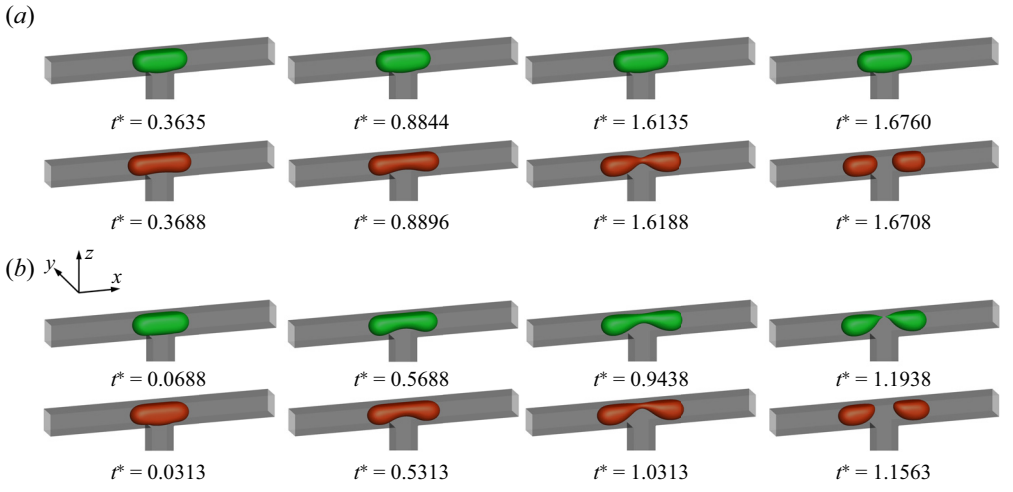

Figure 12. Time evolution of the droplet shapes at (*a*) $Ca = 0.005$ and (*b*) $Ca = 0.03$ for the clean (top row) and surfactant-contaminated systems (bottom row).

droplet tips, the surfactants are swept away from the droplet neck and accumulate at both sides of the droplet tips owing to the high curvature (Liu *et al.* 2018, 2020). As the neck thickness decreases rapidly to a certain value, the droplet upper interface is far from the channel wall (at $t^* = 5.6$). Surfactants accumulate at the droplet neck, where the curvature is higher (Zhang *et al.* 2021*b*). This decreases the interfacial tension in the neck and accelerates the neck contraction process, which can increase the drainage of fluid inside the neck towards the droplet tips. Finally, the droplet breaks up symmetrically into two daughter droplets (at $t^* = 5.7047$).

5.1.2. *Effect of capillary number*

The effect of the capillary number Ca on the droplet dynamics is studied by increasing Ca from 0.005 with an increment of 0.005, where the bulk surfactant concentration and dimensionless initial droplet length are fixed at $\psi_b = 0.1$ and $l_0^* = 1.5$, respectively. Figure 12 presents the time evolution of the droplet shapes at (*a*) $Ca = 0.005$ and (*b*) $Ca = 0.03$ for the clean (top row) and surfactant-contaminated systems (bottom row). At a small value of Ca, i.e. $Ca = 0.005$, the clean droplet eventually stays at the T-junction without forming a neck (the top row of figure 12*a*), while the surfactant-contaminated droplet forms a neck and eventually splits into two daughter droplets with equal volume (the bottom row of figure 12*a*). At the median value of Ca, i.e. $Ca = 0.01$, the clean and surfactant-contaminated droplets both break up, but the surfactant-contaminated droplet breaks up earlier than the clean droplet (figure 4*b*). At a large value of Ca, i.e. $Ca = 0.03$, the clean and surfactant-contaminated droplets both break up, and the breakup time of the two droplets nearly coincide (figure 12*b*). These phenomena indicate that the presence of surfactants promotes the droplet breakup at low values of Ca and reduces the breakup time of the droplet neck at median values of Ca, but has little effect on the droplet breakup at high values of Ca.

Figure 13 presents the time evolution of the dimensionless neck thickness δ^* at different values of Ca for (*a*) the clean and (*b*) surfactant-contaminated systems. At the smallest capillary number, i.e. $Ca = 0.005$, the value of δ^* remains approximately 1 in the clean system, but decreases to 0 in the surfactant-contaminated system. We also note that the

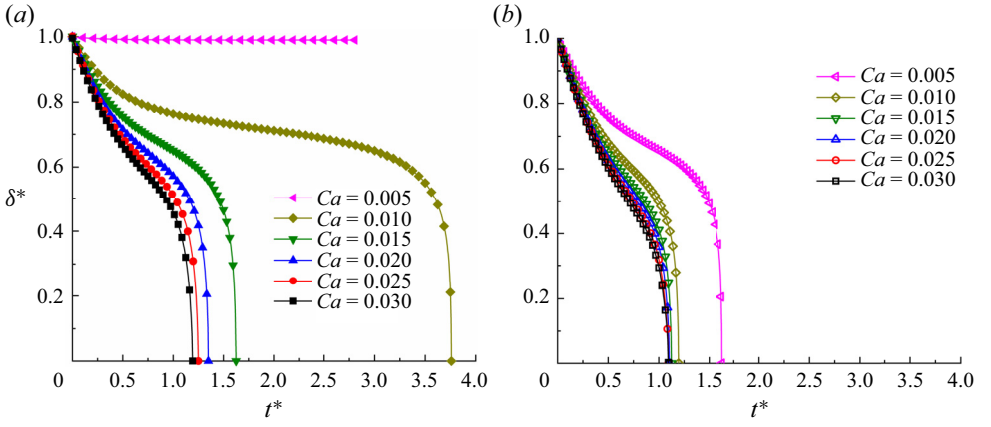

Figure 13. Dimensionless neck thickness δ^* as a function of the dimensionless time t^* at different capillary numbers for the (*a*) clean and (*b*) surfactant-contaminated systems.

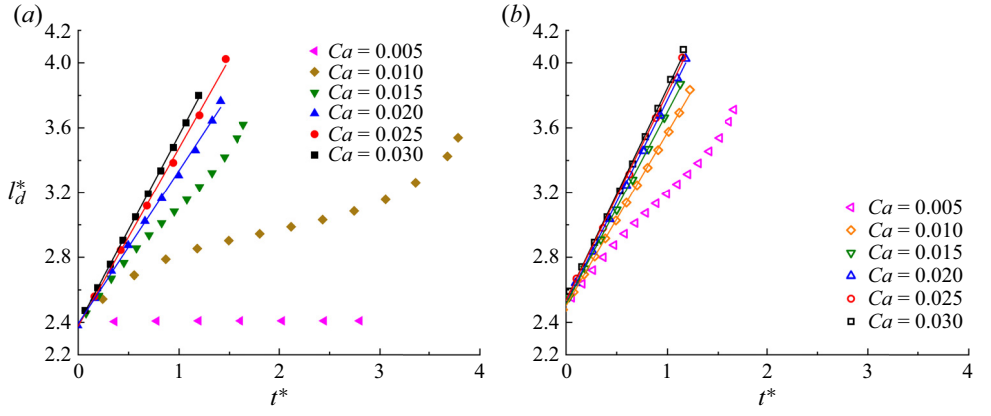

Figure 14. Time evolution of the dimensionless droplet length l_d^* under different capillary numbers Ca for the (*a*) clean and (*b*) surfactant-contaminated systems.

breakup time of the droplet neck, i.e. the time when δ^* decreases to 0, occurs earlier in the surfactant-contaminated system than that in the clean system at the same Ca. These phenomena indicate that the presence of surfactants promotes the droplet breakup. In both the clean and surfactant-contaminated systems, the curves of δ^* varying with t^* gradually coincide as Ca increases. It also can be observed in the surfactant-contaminated system that the curves of δ^* with t^* nearly coincide when $Ca \geq 0.02$ (figure 12*b*).

The degree of blockage of the droplet to the branch channels is described by the time evolution of the dimensionless droplet length l_d^* under different values of the capillary number Ca, as shown in Figure 14. In the figure, the straight lines represent the fitting lines. For the clean system (figure 14*a*), l_d^* increases linearly with t^* when $Ca \geq 0.02$, and the slopes of the fitting lines are 0.9438, 1.0989 and 1.1690 for $Ca = 0.02$, 0.025 and 0.03, respectively. For the surfactant-contaminated system (figure 14*b*), l_d^* increases linearly with t^* when $Ca \geq 0.01$, and the slopes of the fitting lines are 1.0690, 1.1861, 1.2594, 1.2812 and 1.3095 for $Ca = 0.01$, 0.015, 0.02, 0.025 and 0.03, respectively. In both the clean and surfactant-contaminated systems, the slope of the fitting line gradually increases as Ca increases, and the rate of increase in the fitting line slope decreases as

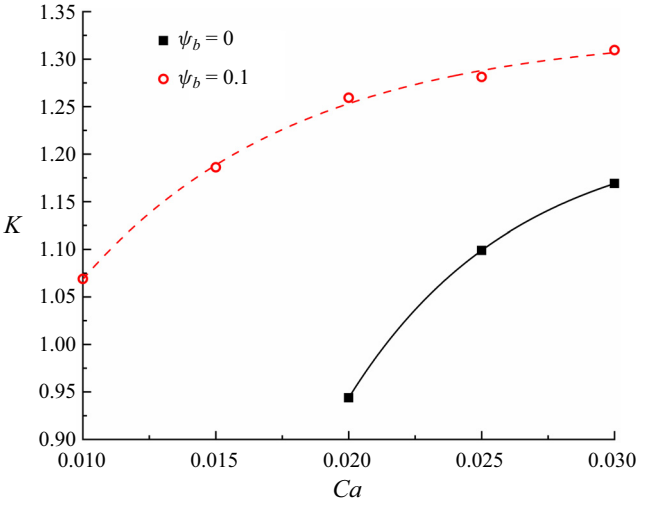

Figure 15. Slopes of the fitting lines (K) as a function of the capillary number Ca for both the clean and surfactant-contaminated systems. The solid black and dashed red lines represent the fitting lines for the clean and surfactant-contaminated systems, respectively.

Ca increases. This indicates that the ratio of the maximum droplet area to the branch channel area in the y–z plane (α) decreases as Ca increases, and the rate of decrease in α decreases as Ca increases. As Ca increases, the fitting lines gradually approach each other in both the clean and surfactant-contaminated systems, suggesting that α tends towards a certain value. Consequently, the curves of δ^* varying with t^* gradually approach each other as Ca increases in the two systems (figure 13*a*,*b*). Moreover, in the surfactant-contaminated system, the values of l_d^* are almost equal when $Ca \geq 0.02$, thus causing the curves of δ^* varying with t^* to coincide when $Ca \geq 0.02$ (figure 13*b*).

When the branch channels are completely blocked by the droplet, the dimensionless droplet length l_d^* increases linearly with the dimensionless time t^* (figure 14), such that the two formulas could be found to predict the variation of l_d^* with t^* in both the clean and surfactant-contaminated systems. Figure 15 presents the plots of the slopes of the fitting lines (K) as a function of the capillary number Ca when the branch channels are completely blocked by the droplet for the two systems, where the red dashed and black solid lines indicate the fitting lines. The expressions of the fitting lines are $K = 1.2268 - 6.7823 \times \mathrm{e}^{-t^*/0.0063}$ and $K = 1.3288 - 0.8952 \times \mathrm{e}^{-t^*/0.0081}$ for the clean and surfactant-contaminated systems, respectively. This indicates that the dimensionless droplet length can be predicted by $l_d^* = l_{d0}^* + Kt^*$, where $l_{d0}^* = 2.4$ and $K = 1.2268 - 6.7823 \times \mathrm{e}^{-t^*/0.0063}$ for the clean system, while $l_{d0}^* = 2.45$ and $K = 1.3288 - 0.8952 \times \mathrm{e}^{-t^*/0.0081}$ for the surfactant-contaminated system. We also note that the values of K are greater in the surfactant-contaminated system than that in the clean system at the same Ca. At a fixed value of Ca, the accumulation of surfactants at the droplet tips causes the droplet to deform, which promotes the flow of the droplet in the region of low resistance, i.e. in the region away from the microchannel wall. Therefore, the droplet length increases faster in the surfactant-contaminated system than that in the clean system.

Figure 16 presents the evolution of the neck breakup time t_{break}^* with the capillary number Ca for both the clean and surfactant-contaminated systems. In the clean system ($\psi_b = 0$), t_{break}^* decreases monotonically as Ca increases. As Ca increases, the inertial

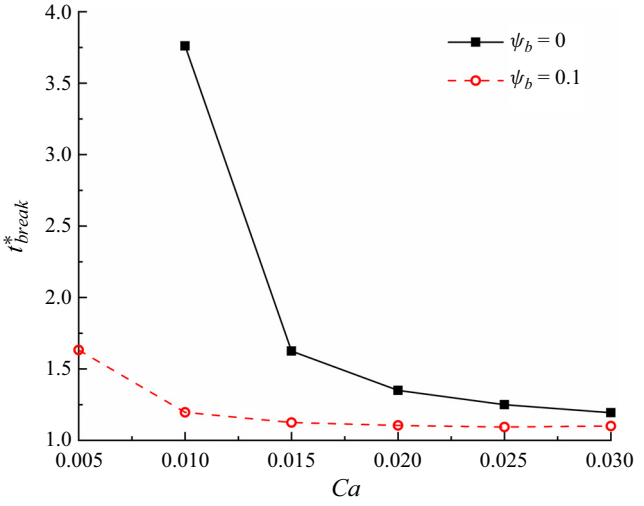

Figure 16. Breakup time of the droplet neck (t^*_{break}) as a function of the capillary number Ca for both the clean and surfactant-contaminated systems.

effect increases, which intensifies the compression of the injected fluid on the droplet neck, resulting in a reduced breakup time. In the surfactant-contaminated system ($\psi_b = 0.1$), t^*_{break} first monotonically decreases and then remains nearly unchanged as Ca increases. The reason for the former decrease is the same as that described in the case of the clean system. The later near-constant value of t^*_{break} when $Ca \geq 0.02$ can be explained as follows: as Ca increases, the surfactants absorbed at the droplet interface are significantly diluted, which is because the deformation rate of the droplet interface increases (see the comparison of figure 12*a*,*b*). Thus, t^*_{break} increases because the surfactant effect is weakened. Moreover, the inertial effect increases as Ca increases, which causes t^*_{break} to decrease. As a result, the two opposite effects cause t^*_{break} to remain almost constant. With an increase in Ca, the difference in t^*_{break} between the clean and surfactant-contaminated systems gradually decreases. As Ca increases, the inertial effect gradually increases, and the surfactant role is thus correspondingly weakened.

5.2. *Asymmetric boundary condition*

This subsection presents an examination of the effect of surfactants on a droplet flowing through a T-junction microchannel under asymmetric boundary conditions ($P^*_1 \neq P^*_2$), where the surfactant role is determined by comparing the droplet morphology, volume ratio of the generated daughter droplets (V_1/V_2) and dimensionless breakup time of the droplet neck (t^*_{break}) under different values of the dimensionless pressure difference ΔP^* and bulk surfactant concentration ψ_b.

5.2.1. *Effect of pressure difference*

The effect of the surfactants on the droplet flowing through a T-junction microchannel under different values of pressure difference ΔP^* is investigated by increasing ΔP^* from 0 to 3.33×10^{-3}. Different values of ΔP^* are obtained on decreasing the pressure applied at the right branch outlet, while maintaining the pressure applied at the left branch outlet at a constant. Figure 17 presents the time evolution of the droplet shape at (*a*) $\Delta P^* = 1 \times 10^{-6}$, (*b*) $\Delta P^* = 3.33 \times 10^{-6}$ and (*c*) $\Delta P^* = 1 \times 10^{-3}$ for the clean (top row) and

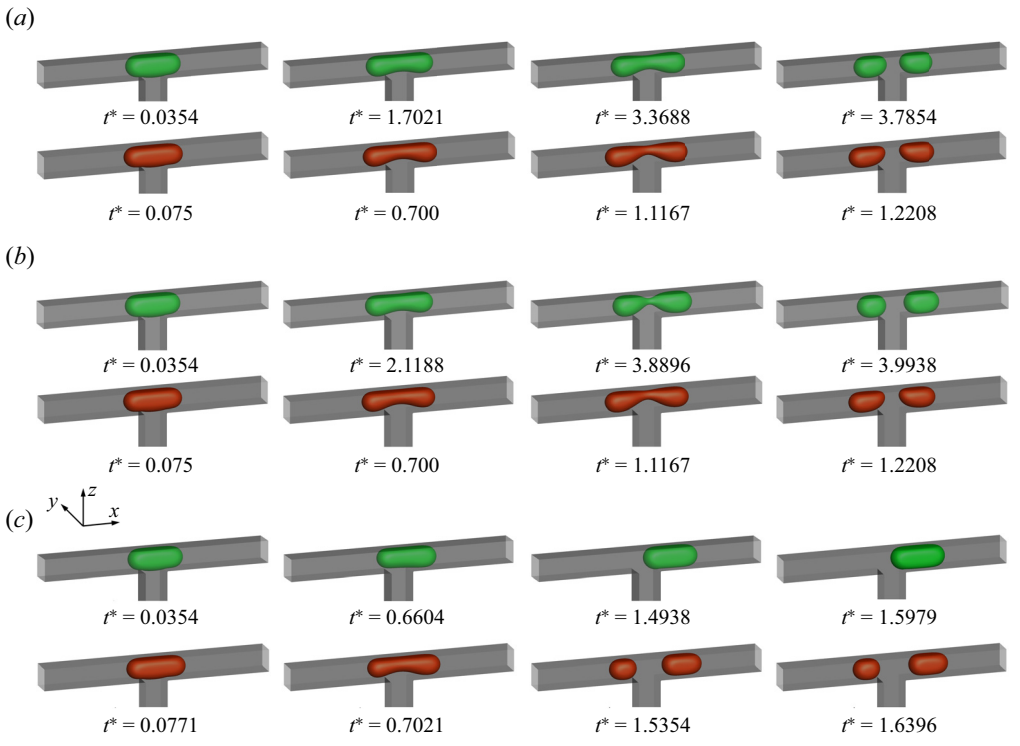

Figure 17. Snapshots of the droplet flowing through a T-junction microchannel at (*a*) $\Delta P^* = 1 \times 10^{-6}$, (*b*) $\Delta P^* = 3.33 \times 10^{-6}$ and (*c*) $\Delta P^* = 1 \times 10^{-3}$ for the clean (top row) and surfactant-contaminated systems (bottom row). The other parameters are considered as $Ca = 0.01$, $l_0^* = 1.5$ and $\psi_b = 0.1$.

surfactant-contaminated systems (bottom row). At $\Delta P^* = 1 \times 10^{-6}$ (figure 17*a*), the clean and surfactant-contaminated droplets both break up into two daughter droplets of similar volumes. The breakup time of the droplet neck is smaller in the surfactant-contaminated system than that in the clean system. We also note that the droplet length appears to be larger in the surfactant-contaminated system than that in the clean system. When the pressure difference is increased to $\Delta P^* = 3.33 \times 10^{-6}$ (figure 17*b*), the clean droplet asymmetrically breaks up into two daughter droplets with unequal volumes (shown in the top row), while the surfactant-contaminated droplet still breaks up into two daughter droplets with similar volumes (see the bottom row). The surfactant-contaminated droplet breaks up earlier than the clean droplet. As in the case of $\Delta P^* = 1 \times 10^{-6}$, the length of the surfactant-contaminated droplet is also greater than that of the clean droplet. Upon further increasing ΔP^* to 1×10^{-3} (figure 17*c*), the clean droplet completely enters the right branch channel without any breakup (top row of figure 17*c*), while the surfactant-contaminated droplet breaks up into two daughter droplets of unequal volumes (bottom row of figure 17*c*). These phenomena indicate that the presence of surfactants not only decreases the droplet breakup time, but also promotes the droplet to break up under asymmetric boundary condition.

Figure 18 presents the volume ratio of the two daughter droplets (V_1/V_2) as a function of the dimensionless pressure difference ΔP^* for the clean (solid lines with square symbols) and surfactant-contaminated system (dashed line with circle symbols). It should be noted that $V_1/V_2 = 0$ and 1 respectively indicate that the droplet flows entirely through the right

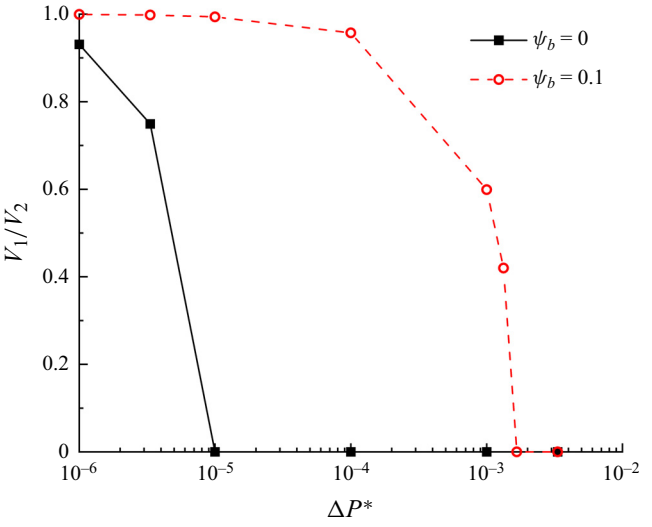

Figure 18. Volume ratio of the two daughter droplets (V_1/V_2) as a function of the dimensionless pressure difference ΔP^* for the clean and surfactant-contaminated systems.

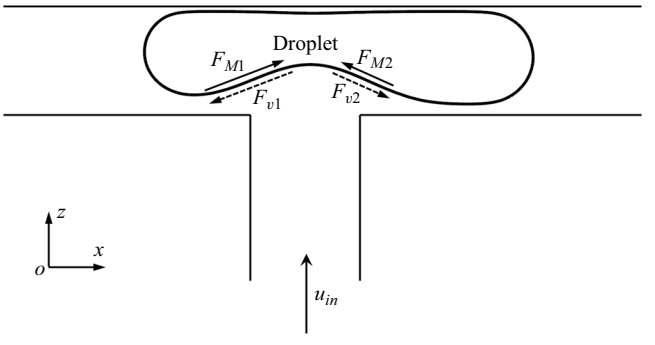

Figure 19. Schematic of surfactant-contaminated droplet passing through a T-junction microchannel in the x–z middle plane under asymmetric boundary conditions.

branch channel and that the volumes of the two daughter droplets are identical. In both the clean and surfactant-contaminated systems, V_1/V_2 monotonically decreases to zero as ΔP^* increases, and this rate of decrease is higher in the clean system. This indicates that the presence of surfactants could decrease the pressure difference between the droplet tips. In the range of ΔP^* varying from 1×10^{-6} to 1×10^{-4}, the value of V_1/V_2 is closer to 1 in the surfactant-contaminated system than that in the clean system at the same value of ΔP^*. This means that the presence of surfactants could promote the breakup of the droplets into two daughter droplets of equal volume. In the surfactant-contaminated system, the value of V_1/V_2 also decreases to 0 at $\Delta P^* = 1.67 \times 10^{-3}$, suggesting that the effect of surfactants on the asymmetric droplet breakup is negligible.

To elucidate the effect of surfactants on the droplet asymmetric breakup under asymmetric boundary conditions, figure 19 presents the plots of the effects of the Marangoni stresses (F_{M1} and F_{M2}) and additional viscous drag stresses (F_{v1} and F_{v2}) on the neck contraction process. As shown in this figure, the blockage degree of the right branch channel is more serious than that of the left branch channel, which is due to the

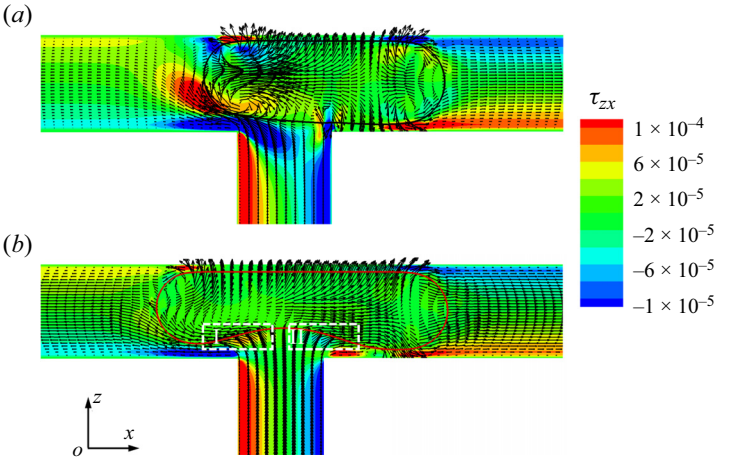

Figure 20. Velocity vectors and the distribution of the shear stress τ_{zx} in the x–z middle plane at $t^* = 0.4938$ for the (a) clean and (b) surfactant-contaminated systems. The black and red curves indicate the clean and surfactant-contaminated droplet interfaces, respectively. The other parameters considered are $Ca = 0.01$, $\psi_b = 0.1$, $l_0^* = 1.5$ and $\Delta P^* = 10^{-3}$.

lower pressure applied at the right branch outlet. This causes more continuous fluid to flow through the left branch channel, which results in a higher flow rate near the droplet bottom interface in the left branch channel than that near the droplet bottom interface in the right branch channel (top row of figure 22). In the presence of surfactants, the continuous fluid sweeps more surfactants towards the left side of the droplet bottom interface, which causes more surfactants to accumulate at the left side of the droplet bottom interface (bottom row of figure 22). Meanwhile, the surfactant concentration at the left side of the droplet bottom interface is more uneven than that at the right side of the droplet bottom interface, which is due to the higher flow rate near the droplet bottom interface in the left branch channel. This causes the Marangoni stress generated at the left side of the droplet bottom interface F_{M1} to be greater than that generated at the right side of the droplet bottom interface F_{M2}, i.e. $F_{M1} > F_{M2}$. To balance the Marangoni stresses, two viscous drag stresses, i.e. F_{v1} and F_{v2}, are induced, and they act at the droplet interface in the direction opposite to that of the Marangoni stresses (dashed arrows). Obviously, F_{v1} and F_{v2} cause the droplet interface to stretch towards both sides of the droplet tips. As $F_{v1} > F_{v2}$, the droplet interface is more inclined to deform towards the left branch channel outlet, and it is more difficult for the right branch channel to be blocked by the droplet. Meanwhile, owing to the adsorption of surfactants at the droplet interface, the interfacial tension is reduced, thus making it easier for the droplet to deform and reducing the overall blockage of the microchannel. The two aforementioned factors facilitate the decrease in the pressure difference between the droplet tips, which is helpful for generating daughter droplets of equal volume.

Figure 20 presents the velocity vectors and distribution of the shear stress τ_{zx} in the x–z middle plane at $t^* = 0.4938$ for the (a) clean and (b) surfactant-contaminated systems. In the clean system (figure 20a), a strong shear stress acts on the lower left side of the droplet tip. This creates a vortex on the left side of the droplet, which promotes the droplet flow to the right-branch channel. However, in the surfactant-contaminated system (figure 20b), there are two regions comprising high shear stress near the lower droplet interface (two regions indicated by white dashed lines). The shear stress in region I is higher than that

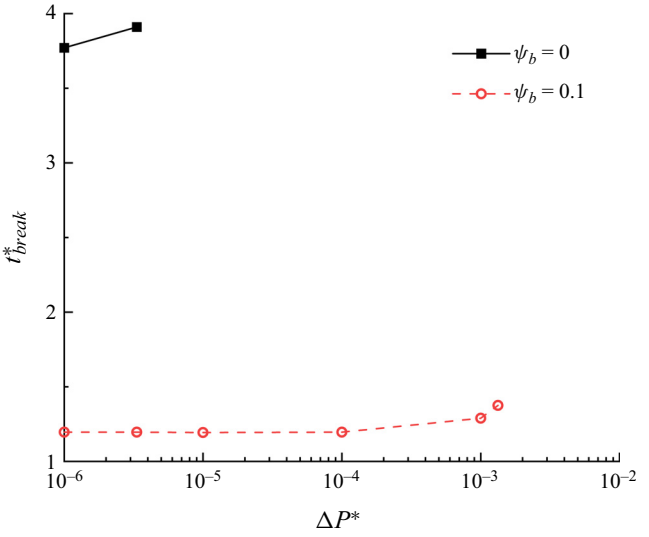

Figure 21. Dimensionless breakup time of the droplet neck (t^*_{break}) as a function of the dimensionless pressure difference ΔP^* for both the clean and surfactant-contaminated systems.

in region II, which stretches the droplet interface towards the left branch channel and facilitates the breakup of the droplet into two daughter droplets of equal volume.

Figure 21 presents the variation in the droplet breakup time t^*_{break} with the pressure difference ΔP^* for both the clean and surfactant-contaminated systems. In the clean system (indicated by the solid line with square symbols), t^*_{break} increases as ΔP^* increases from 1×10^{-6} to 3.33×10^{-6}. When ΔP^* is increased to 3.33×10^{-6}, a broader tunnel is formed between the droplet interface and the left branch channel wall (a comparison between the two top rows is presented in figure 17*a*,*b*), which facilitates the flow of the continuous fluid. This alleviates the compression of the continuous fluid at the droplet neck, thus making it more difficult for the neck to break. In the surfactant-contaminated system (indicated by dashed lines with circles), t^*_{break} initially remains almost constant and then increases as ΔP^* increases. As ΔP^* increases from 1×10^{-6} to 1×10^{-4}, the droplet breaks up almost symmetrically, i.e. the value of V_1/V_2 is close to 1 (figure 18); therefore, the values of t^*_{break} are close to the value of t^*_{break} at the same simulation parameters under symmetric boundary conditions. The reason for the latter increase is the same as that in the case of the clean system. At the same ΔP^*, t^*_{break} is smaller in the surfactant-contaminated system than that in the clean system. The corresponding reasons are presented in figure 11.

Figure 22 presents the distributions of the velocity magnitude (top row) and surfactant concentration (bottom row) at three typical t^* values, where the pressure difference is fixed at $\Delta P^* = 1 \times 10^{-3}$. At $t^* = 0.4938$, the droplet enters the right branch channel (top row of figure 22), which is because the pressure applied at the right branch outlet is lower. Accordingly, the tunnel between the droplet interface and channel wall is broader in the left branch channel than that in the right branch channel, and the position of the droplet neck deviates from the left branch outlet. As the blockage of the droplet to the branch channel is weaker in the left branch channel than that in the right branch channel, the magnitude of the velocity near the left side of the droplet bottom interface is larger than that near the right side of the droplet bottom interface (Chen & Deng 2017). Therefore, more surfactants are swept to the left droplet tip, and the surfactants are more unevenly distributed at the left side of the droplet bottom interface than that at the right side (bottom row in figure 22). As

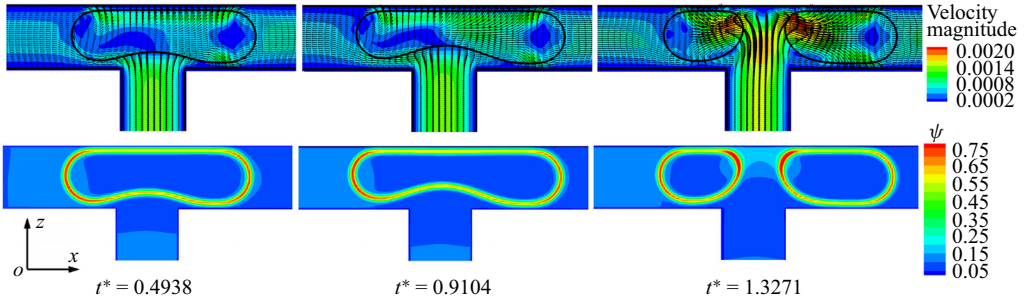

Figure 22. Distributions of the velocity magnitude (top row) and surfactant concentration (bottom row) in the x–z middle plane at three typical t^* values, where the pressure difference is fixed at $\Delta P^* = 1 \times 10^{-3}$. The curved black lines correspond to the droplet interface ($\rho^N = 0$).

t^* increases to 0.9104, the non-uniformity of the surfactants at the left side of the droplet bottom interface increases (a comparison between $t^* = 0.4938$ and 0.9104 is presented), which is due to the intensive velocity magnitude near the left side of the droplet bottom interface. Upon further increasing t^* to 1.3271, the droplet breaks up into two daughter droplets of unequal volume, and the corresponding value of $V_1/V_2 = 1.29$ is obtained. It can also be observed that more surfactants accumulate at the droplet tips where the curvature is high.

5.2.2. *Effect of surfactant concentration*

It has been proved in the above subsection that the presence of surfactants can facilitate droplet breakup into two daughter droplets of equal volume, but the effect of the surfactant concentration on the droplet breakup under asymmetric boundary conditions is still unclear. In addition, it is well known that the excessive addition of surfactants into two-phase systems not only increases toxicity, but also increases separation costs (Sakai 2008; Seok *et al.* 2011; Shimokawa, Ishii & Ohshima 2016); therefore, the determination of the optimal surfactant concentration while balancing the surfactant role and dosage is of great significance. In this subsection, the effect of the bulk surfactant concentration ψ_b on a droplet flowing through a T-junction microchannel is investigated. Figure 23 presents the volume ratio of the two daughter droplets (V_1/V_2) as a function of the bulk surfactant concentration ψ_b, where the inset figures present the shapes obtained after the droplet breaks up or flows through a branch channel. It can be observed from the figure that V_1/V_2 first increases rapidly as ψ_b increases from 0.05 to 0.1, then remains almost constant as ψ_b increases from 0.1 to 0.4 and finally decreases slightly as ψ_b increases from 0.4 to 0.6. The former rapid increase occurs because the additional viscous drag stresses induced by the Marangoni stresses cause the droplet to break up symmetrically (figure 19). The reason for the latter being almost constant is as that, as ψ_b increases, the amount of surfactants absorbed at the left side of the droplet bottom interface increases, thus reducing the interfacial tension. This facilitates droplet deformation and creates a wider tunnel between the left side of the droplet bottom interface and the microchannel wall. As the tunnel width increases, the fluid velocity near the left side of the droplet bottom interface decreases, which alleviates the non-uniformity of the surfactants at the droplet bottom interface. This hinders the increase in Marangoni stresses and additional viscous drag stresses, which prevents V_1/V_2 from increasing further. The final slight decrease can be explained as follows: as ψ_b continuously increases, the absorbed surfactants at the droplet interface increase and reach the CMC (the bottom row of figure 25*b*), which decreases the

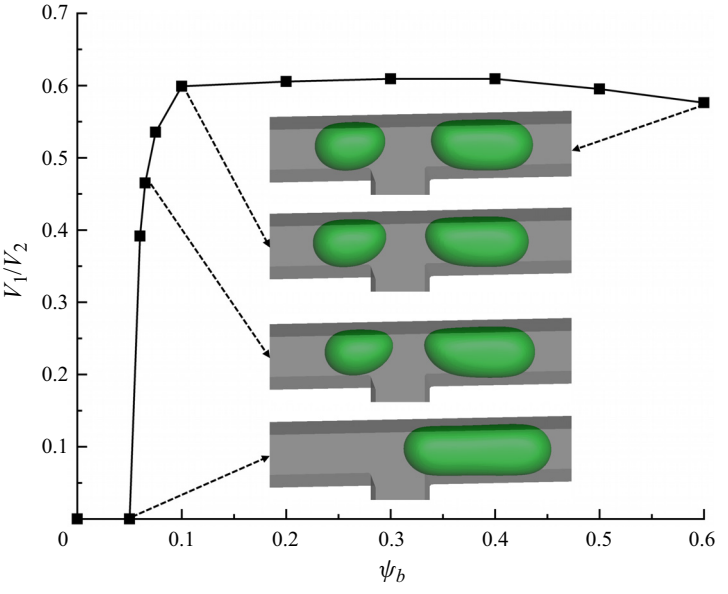

Figure 23. Volume ratio of the two daughter droplets (V_1/V_2) as a function of the bulk surfactant concentration ψ_b, where the illustrations depict the shapes of droplet breakup or droplet flowing through one branch channel. Other parameters are fixed at $Ca = 0.01$, $l_0^* = 1.5$ and $\Delta P^* = 1 \times 10^{-3}$.

interfacial tension gradient at the droplet interface. Therefore, the Marangoni stresses and additional viscous drag stresses correspondingly decrease, which weakens the effect of the surfactants on the asymmetric breakup of the droplet.

Figure 24 presents the dimensionless droplet breakup time t^*_{break} as a function of the bulk surfactant concentration ψ_b. It can be observed from the figure that t^*_{break} first decreases and then increases as ψ_b increases. The reason for the former decrease has been described. The latter increase can be explained as follows: as ψ_b increases, the surfactants absorbed at the droplet interface increase and gradually reach the CMC (bottom rows of figure 25*a*,*b*), which weakens the Marangoni stresses and additional viscous drag stresses. As mentioned above, the additional viscous drag stresses are conducive to droplet breakup, and the weakened viscous drag stresses thus cause t^*_{break} to increase.

Figure 25 presents the distributions of the velocity magnitude (top row) and surfactant concentration (bottom row) for (*a*) $\psi_b = 0.06$ and (*b*) $\psi_b = 0.6$. As ψ_b increases from 0.06 to 0.1 (comparison between figures 22 and 25*a*), the amount of surfactants absorbed at the droplet interface increases, and the uneven distribution of surfactants at the left bottom interface of the droplet becomes more severe. Upon further increasing ψ_b to 0.6 (figure 25*b*), the amount of surfactants absorbed at the droplet interface further increases, while the surfactants at the droplet interface become more evenly distributed. Similar phenomena have been observed in previous studies (Zhang *et al.* 2022, 2023*a*). It should be noted that the CMC is reached, which is given by $\mathrm{CMC} = 1 - \exp[-2/(3E_0)] = 0.74$. This means that the magnitudes of the Marangoni stresses and additional viscous drag stresses first increase and then decrease as ψ_b increases from 0.06 to 0.6.

5.3. *Phase diagram*

To systematically investigate the effect of the surfactants on the asymmetric breakup of the droplet under different parameters, figure 26 presents the phase diagram describing

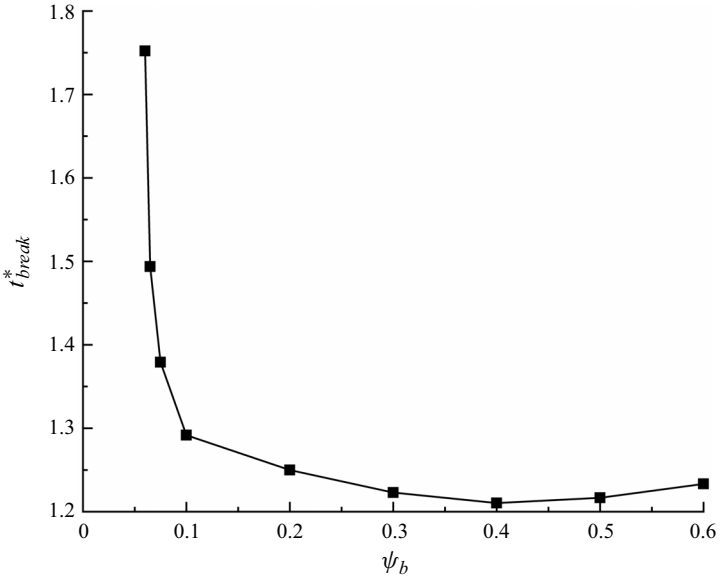

Figure 24. Dimensionless breakup time of the droplet neck (t^*_{break}) as a function of the bulk surfactant concentration ψ_b.

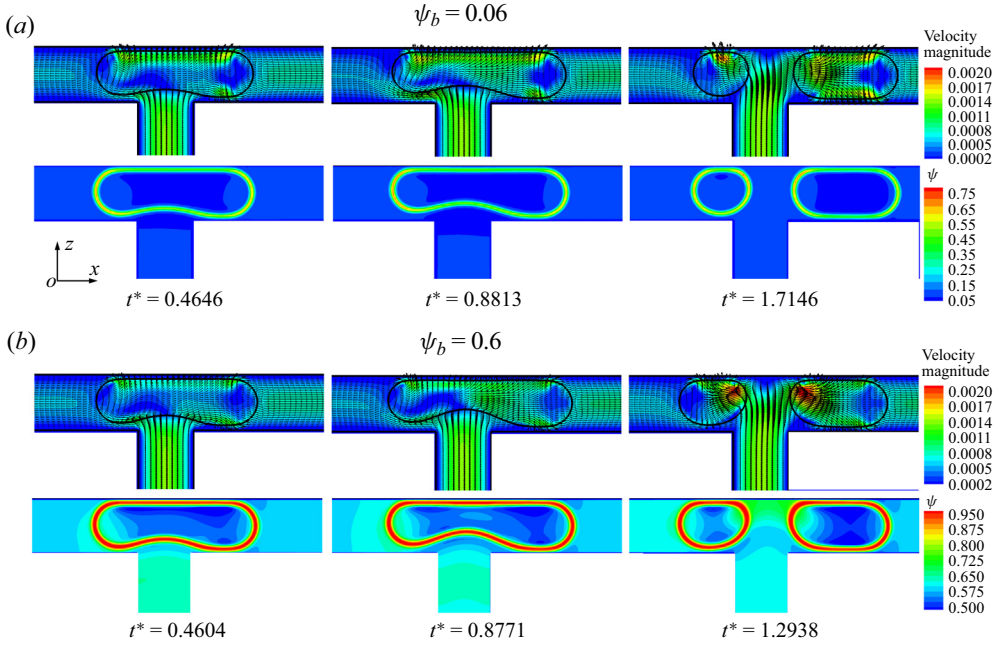

Figure 25. Distributions of the velocity magnitude (top row) and surfactant concentration (bottom row) in the x–z middle plane for different bulk surfactant concentrations ψ_b. The black curved lines correspond to the droplet interfaces.

how the volume ratio of the two daughter droplets (V_1/V_2) varies with the bulk surfactant concentration ψ_b and pressure difference ΔP^*. In this figure, the solid and dashed red lines are the auxiliary lines, which are used to clearly represent the variations of V_1/V_2 with ψ_b and ΔP^*, respectively. In the absence of surfactants, a small pressure difference

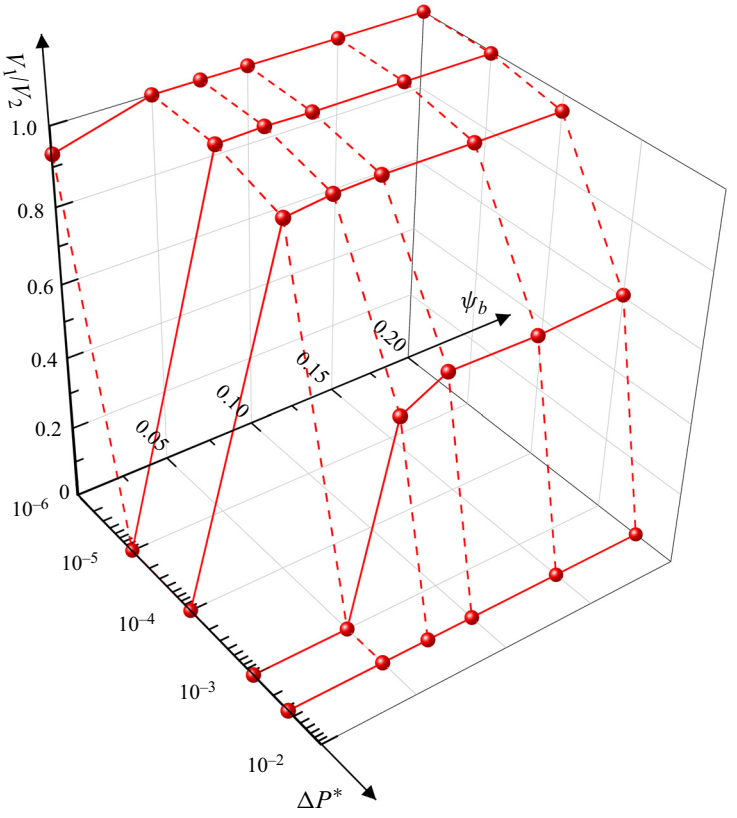

Figure 26. Effects of the bulk surfactant concentration ψ_b and pressure difference ΔP^* on the volume ratio of daughter droplets (V_1/V_2). The solid and dashed red lines indicate the auxiliary lines used to clearly represent the variation in V_1/V_2 with ψ_b and ΔP^*, respectively.

would not cause the droplet to break up but to enter one branch channel instead (dashed red line of $\psi_b = 0$). With the addition of surfactants, the value of V_1/V_2 first remains nearly constant as ΔP^* increases from 1×10^{-6} to 1×10^{-4} and then dramatically decreases and disappears as ΔP^* increases continuously. In the range of $\Delta P^* = 1 \times 10^{-6}$ to 1×10^{-4}, the value of V_1/V_2 rapidly increases as ψ_b increases from 0 to 0.05 and then remains nearly constant as ψ_b continues to increase. As ΔP^* continuously increases to 1×10^{-3}, a higher value of ψ_b is required to obtain a high value of V_1/V_2. However, the value of V_1/V_2 can only be increased to approximately 0.6, even after the addition of surfactants at a high concentration. To obtain two daughter droplets of similar volume, the optimal surfactant concentrations under different values of ΔP^* can be obtained, as shown in figure 26. It can be observed form the figure that the optimal surfactant concentration is approximately 0.05 and 0.1 in the ranges of $\Delta P^* = 1 \times 10^{-6}$ to 1×10^{-4} and $\Delta P^* = 1 \times 10^{-3}$, respectively.

6. Conclusions

In this study, the flow of a surfactant-contaminated droplet in a T-junction microchannel is simulated using our recently developed LB method (Zhang *et al.* 2023*a*). We first studied the effect of the surfactants on the droplet breakup at different values of the dimensionless initial droplet length l_0^* and capillary number Ca under symmetric boundary conditions. At small and moderate l_0^* values, the branch channels are partially blocked by the droplet,

and the surfactants are unevenly distributed at the droplet interface owing to the flow of continuous fluid in the tunnel between the droplet bottom interface and the microchannel wall. Additional viscous drag stresses are induced to balance the Marangoni stresses, which promote the droplet deformation and breakup. However, at large l_0^* values, the branch channels are completely blocked by the droplet, and the neck contraction process is determined by the injection rate of the continuous fluid; thus, the surfactant effect is significantly weakened. When the branch channels are completely blocked by the droplet, the dimensionless droplet length l_d^* increases linearly with the dimensionless time t^*, and the rate of increase depends on the injection rate of the continuous fluid (quantified by Ca) and the ratio of the maximum droplet area to the channel area in the y–z plane (α). Based on this, two formulas are developed to predict the evolution of l_d^* with t^* for both the clean and surfactant-contaminated systems. At a fixed Ca, the increasing rate of l_d^* is higher in the surfactant-contaminated system than in the clean system because of the smaller value of α in the surfactant-contaminated system.

We then studied the effect of the surfactants on droplet breakup under different values of pressure difference ΔP^* and bulk surfactant concentration ψ_b under asymmetric boundary conditions. As ΔP^* increases, the volume ratio of the generated droplets (V_1/V_2) decreases to zero in both systems, whereas this rate of decrease is lower in the surfactant-contaminated system. The presence of surfactants decreases the interfacial tension and generates asymmetric Marangoni stresses, which are conducive to reducing the overall blockage of the microchannels. Therefore, the pressure difference between the droplet tips decreases, which is helpful for generating daughter droplets of equal volume. Under the influence of ΔP^*, the droplet deforms asymmetrically at the T-junction, and the velocity magnitudes near the left and right sides of the bottom interface of the droplet are different. Two unequal Marangoni stresses and two additional unequal viscous drag stresses are asymmetrically generated at the left and right sides of the droplet bottom interface, which prevent the asymmetric deformation and breakup of the droplet interface. As ψ_b increases, V_1/V_2 first increases rapidly, then remains constant and finally decreases slightly.

Finally, we establish a phase diagram to describe how V_1/V_2 varies with ΔP^* and ψ_b. In the range of $\Delta P^* = 1 \times 10^{-6}$ to 1×10^{-4}, V_1/V_2 increases rapidly as ψ_b increases from 0 to 0.05 and then remains nearly constant as ψ_b continues to increase. As ΔP^* increases continuously to 1×10^{-3}, a higher value of ψ_b is required to obtain a high V_1/V_2 value. However, the value of V_1/V_2 can only be increased to approximately 0.6 even after the addition of surfactants at a high concentration.

It is worth noting that the droplet elongation is attributed to two factors, i.e. the drainage of the fluid inside the neck towards the droplet tips and the enhanced shear stresses due to the presence of surfactants. Thus, in our future research, we intend to develop an appropriate method of determining the contribution of the two aforementioned factors. In addition, we intend to adopt a grid refinement technique (Chen *et al.* 2006; Geier, Greiner & Korvink 2009; Huang & Wu 2016) to accurately capture the evolution of the droplet neck in the fracture stage.

Funding. The authors acknowledge the financial support provided by the National Natural Science Foundation of China (no. 52306202).

Declaration of interests. The authors report no conflict of interest.

Author ORCIDs.
Jinggang Zhang https://orcid.org/0009-0007-1964-7399;
Haihang Cui https://orcid.org/0000-0002-0334-6272.

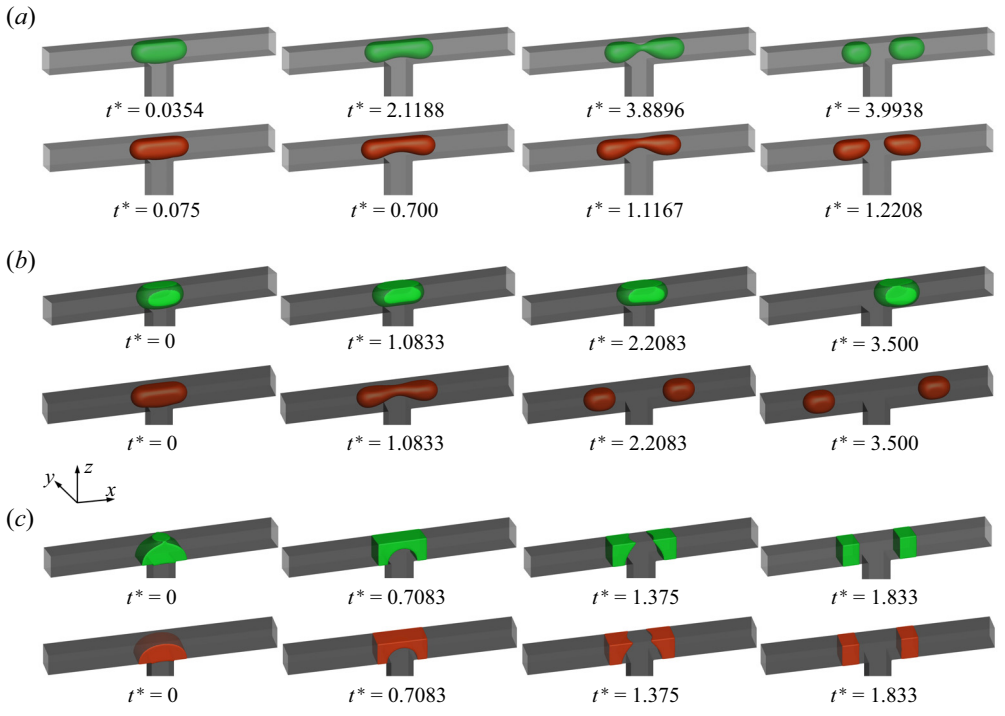

Figure 27. Temporal evolution of the droplet interface ($\rho^N = 0$) at (*a*) $\theta_0 = 0$, (*b*) $\theta_0 = \pi/6$ and (*c*) $\theta_0 = \pi/2$ for the clean (top row) and surfactant-contaminated systems (bottom row). The clean droplet interfaces, surfactant-contaminated droplet interfaces and microchannel walls are indicated in green, red and grey, respectively. The other parameters are $Ca = 0.01$, $l_0^* = 1.5$, $\psi_b = 0.1$ and $\Delta P^* = 3.33 \times 10^{-6}$.

Appendix. Effects of surface wettability and aspect ratio ($\chi = W/H$)

The effect of contact angle θ_0 on a droplet flowing through a T-junction device is studied. Figure 27 presents the temporal evolution of the droplet interface ($\rho^N = 0$) at (*a*) $\theta_0 = 0$, (*b*) $\theta_0 = \pi/6$ and (*c*) $\theta_0 = \pi/2$ for the clean (top row) and surfactant-contaminated systems (bottom row). The other parameters considered are $Ca = 0.01$, $l_0^* = 1.5$, $\psi_b = 0.1$ and $\Delta P^* = 3.33 \times 10^{-6}$. For $\theta_0 = 0$ (figure 27*a*), the clean droplet breaks up into two daughter droplets of different volumes, while the surfactant-contaminated droplet breaks up into two daughter droplets of similar volumes. We also observe that the breakup of the droplet neck occurs earlier in the surfactant-contaminated system than in the clean system. When θ_0 is increased to $\pi/6$ (figure 27*b*), the clean droplet is adsorbed on the microchannel wall, which alleviates the blockage of the microchannel by the droplet. Two non-uniform shear stresses are applied to the two sides of the clean droplet, and the droplet flows through the right branch channel. However, the surfactant-contaminated droplet also breaks up into two daughter droplets, which is similar to the surfactant-contaminated case at $\theta_0 = 0$. This is because the presence of surfactants not only decreases the interfacial tension, but also reduces the contact angle for hydrophilic microchannel walls. Upon further increasing θ_0 to $\pi/2$ (figure 27*c*), the clean and surfactant-contaminated droplets completely block the microchannel and eventually break up into two daughter droplets of similar volumes.

Figure 28 presents the volume ratio of the two daughter droplets (V_1/V_2) as a function of the contact angle θ_0 for the clean (squares with solid lines) and surfactant-contaminated

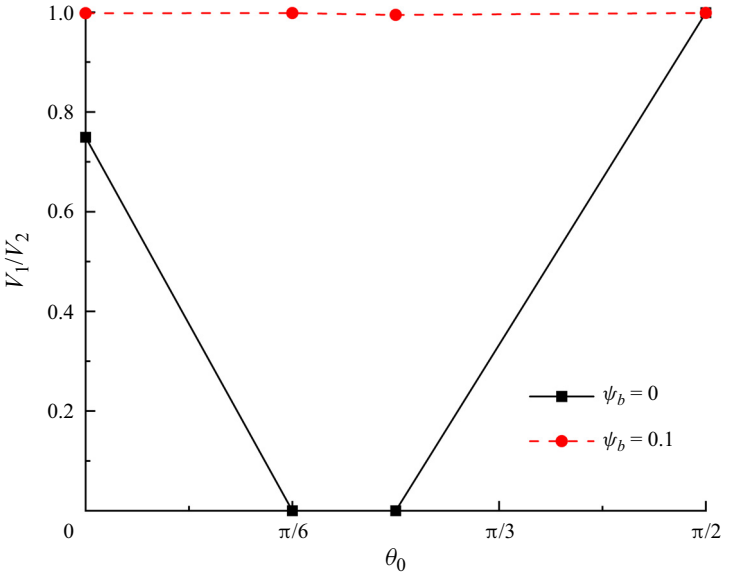

Figure 28. Effect of contact angle θ_0 on the volume ratio of the two daughter droplets (V_1/V_2) for both the clean ($\psi_b = 0$) and surfactant-contaminated systems ($\psi_b = 0.1$). The other parameters are fixed at $Ca = 0.01$, $l_0^* = 1.5$, $\psi_b = 0.1$ and $\Delta P^* = 3.33 \times 10^{-6}$.

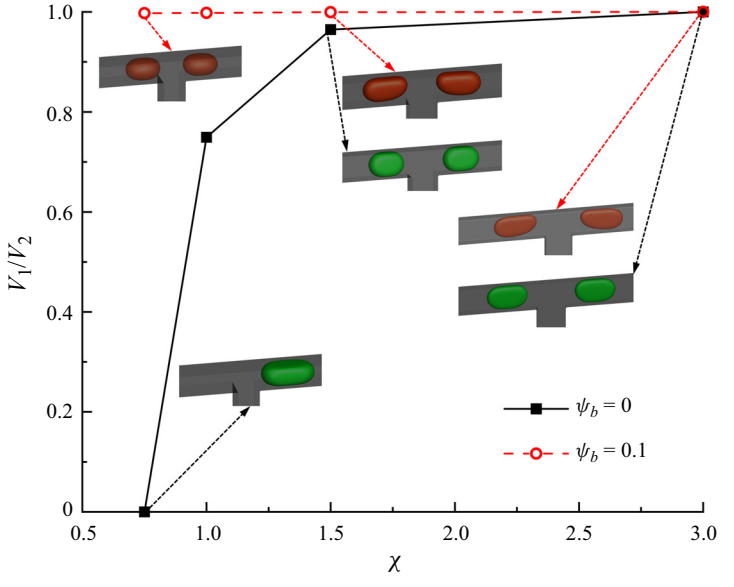

Figure 29. Volume ratio of the two daughter droplets (V_1/V_2) as a function of the aspect ratio χ ($\chi = W/H$). The illustrations show the droplet shapes; the interfaces of the clean and surfactant-contaminated droplets are indicated in green and red, respectively. The other parameters considered are $Ca = 0.01$, $l_0^* = 1.5$ and $\Delta P^* = 1 \times 10^{-5}$.

systems (circles with dashed lines). In the surfactant-contaminated system, V_1/V_2 remains almost constant. However, in the clean system, V_1/V_2 decreases as θ_0 increases from 0 to $\pi/6$, while V_1/V_2 increases as θ_0 increases from$\pi/4$ to $\pi/2$.

Figure 29 presents the effect of the aspect ratio χ ($\chi = W/H$) on the volume ratio of the two daughter droplets (V_1/V_2), where four different values of χ, that is $\chi = 0.75$, 1, 1.5 and 3, were studied. In the surfactant-contaminated system (circles with dashed lines), V_1/V_2 remains nearly constant as χ increases. However, in the clean system (indicated by the squares with solid lines), V_1/V_2 increases monotonically as χ increases. This phenomenon can be explained as follows: as χ increases, the tunnel between the droplet interface and the microchannel wall is reduced, and the non-uniform shear stresses acting on both sides of the droplet interface are weakened, thus causing the droplet to break up symmetrically.

References

Akai, T., Bijeljic, B. & Blunt, M.J. 2018 Wetting boundary condition for the color-gradient lattice Boltzmann method: validation with analytical and experimental data. *Adv. Water Resour.* **116**, 56–66.

Baret, J.-C., Kleinschmidt, F., Harrak, A.E. & Griffiths, A.D. 2009 Kinetic aspects of emulsion stabilization by surfactants: a microfluidic analysis. *Langmuir* **25**, 6088–6093.

Chagot, L., Quilodrán-Casas, C., Kalli, M., Kovalchuk, N.M., Simmons, M.J.H., Matar, O.K., Arcucci, R. & Angeli, P. 2022 Surfactant-laden droplet size prediction in a flow-focusing microchannel: a data-driven approach. *Lab on a Chip* **22**, 3848–3859.

Chen, H., Filippova, O., Hoch, J., Molvig, K., Shock, R., Teixeira, C. & Zhang, R. 2006 Grid refinement in lattice Boltzmann methods based on volumetric formulation. *Physica* A **362**, 158–167.

Chen, X., Xue, C. & Hu, G. 2019 Confinements regulate capillary instabilities of fluid threads. *J. Fluid Mech.* **873**, 816–834.

Chen, Y. & Deng, Z. 2017 Hydrodynamics of a droplet passing through a microfluidic T-junction. *J. Fluid Mech.* **819**, 401–434.

Fu, T., Ma, Y. & Li, H.Z. 2014 Hydrodynamic feedback on bubble breakup at a T-junction within an asymmetric loop. *AIChE J.* **60**, 1920–1929.

Geier, M., Greiner, A. & Korvink, J.G. 2009 Bubble functions for the lattice Boltzmann method and their application to grid refinement. *Eur. Phys. J.* **171**, 173–179.

Gimondi, S., Ferreira, H., Reis, R.L. & Neves, N.M. 2023 Microfluidic devices: a tool for nanoparticle synthesis and performance evaluation. *ACS Nano* **17**, 14205–14225.

Giuffrida, M.C., Cigliana, G. & Spoto, G. 2018 Ultrasensitive detection of lysozyme in droplet-based microfluidic devices. *Biosens. Bioelectr.* **104**, 8–14.

Hafen, N., Thieringer, J.R.D., Meyer, J., Krause, M.J. & Dittler, A. 2023 Numerical investigation of detachment and transport of particulate structures in wall-flow filters using lattice Boltzmann methods. *J. Fluid Mech.* **956**, A30.

Hoang, D.A., Haringa, C., Portela, L.M., Kreutzer, M.T., Kleijn, C.R. & van Steijn, V. 2014 Design and characterization of bubble-splitting distributor for scaled-out multiphase microreactors. *Chem. Engng J.* **236**, 545–554.

Hoang, D.A., Portela, L.M., Kleijn, C.R., Kreutzer, M.T. & van Steijn, V. 2013 Dynamics of droplet breakup in a T-junction. *J. Fluid Mech.* **717**, R4.

Huang, R. & Wu, H. 2016 Total enthalpy-based lattice Boltzmann method with adaptive mesh refinement for solid-liquid phase change. *J. Fluid Mech.* **315**, 65–83.

Jiang, F., Yang, J., Boek, E. & Tsuji, T. 2021 Investigation of viscous coupling effects in three-phase flow by lattice Boltzmann direct simulation and machine learning technique. *Adv. Water Resour.* **147**, 103797.

Kalli, M. & Angeli, P. 2022 Effect of surfactants on drop formation flow patterns in a flow-focusing microchannel. *Chem. Engng J.* **253**, 117517.

Leshansky, A.M., Afkhami, S., Jullien, M.C. & Tabeling, P. 2012 Obstructed breakup of slender drops in a microfluidic T junction. *Phys. Rev. Lett.* **108**, 264502.

Leshansky, A.M. & Pismen, L.M. 2009 Breakup of drops in a microfluidic T junction. *Phys. Fluids* **21**, 023303.

Liang, H., Shi, B.C., Guo, Z. & Chai, Z.H. 2014 Phase-field-based multiple-relaxation-time lattice Boltzmann model for incompressible multiphase flows. *Phys. Rev.* E **89**, 053320.

Liu, H., Ba, Y., Wu, L., Li, Z., Xi, G. & Zhang, Y. 2018 A hybrid lattice Boltzmann and finite difference method for droplet dynamics with insoluble surfactants. *J. Fluid Mech.* **837**, 381–412.

LIU, H., ZHANG, J., BA, Y., WANG, N. & WU, L. 2020 Modelling a surfactant-covered droplet on a solid surface in three-dimensional shear flow. *J. Fluid Mech.* **897**, A33.

NIX, C., GHASSEMI, M., CROMMEN, J. & FILLET, M. 2022 Overview on microfluidics devices for monitoring brain disorder biomarkers. *Trends Anal. Chem.* **155**, 116693.

PAN, K.-L., TSENG, Y.-H., CHEN, J.-C., HUANG, K.-L., WANG, C.-H. & LAI, M.-C. 2016 Controlling droplet bouncing and coalescence with surfactant. *J. Fluid Mech.* **799**, 603–636.

PLATEAU, J. 1873 *Experimental and Theoretical Steady State of Liquids Subjected to Nothing but Molecular Forces*. Gauthiers-Villars.

RAYLEIGH, L. 1878 On the instability of jets. *Proc. Lond. Math. Soc.* **10**, 4–13.

RIAUD, A., ZHANG, H., WANG, X., WANG, K. & LUO, G. 2018 Nemerical study of surfactant dynamics during emulsification in a T-junction microchannel. *Langmuir* **34**, 4980–4990.

SAKAI, T. 2008 Surfactant-free emulsions. *Curr. Opin. Colloid Interface Sci.* **13**, 228–235.

SAMIE, M., SALARI, A. & SHAFII, M.B. 2013 Breakup of microdroplets in asymmetric T junctions. *Phys. Rev.* E **87**, 053003.

SEOK, S.-J., PARK, J.-S., HONG, J.-R., GIL, H.-W., YANG, J.-O., LEE, E.-Y., SONG, H.-Y. & SONG, S.-Y. 2011 Surfactant volume is an essential element in human toxicity in acute glyphosate herbicide intoxication. *Clin. Toxicol.* **49**, 892–899.

SHARMA, B. & SHARMA, A. 2022 Microfluidics: recent advances toward lab-on-chip applications in bioanalysis. *Adv. Engng Mater.* **24**, 2100738.

SHIMOKAWA, K., ISHII, F. & OHSHIMA, H. 2016 Physicochemical properties and clinical applications of surfactant-free emulsions prepared with electrolytic reduction ion water (Eri). In *Encyclopedia of Biocolloid and Biointerface Science 2V Set*, pp. 451–458. John Wiley & Sons.

SOLIGO, G., ROCCON, A. & SOLDATI, A. 2019 Coalescence of surfactant-laden drops by phase field method. *J. Fluid Mech.* **376**, 1292–1311.

SOLIGO, G., ROCCON, A. & SOLDATI, A. 2020 Deformation of clean and surfactant-laden droplets in shear flow. *Meccanica* **55**, 371–386.

STONE, H.A., BENTLEY, B.J. & LEAL, L.G. 1986 An experimental study of transient effects in the breakup of viscous drops. *J. Fluid Mech.* **173**, 131–158.

SUN, G., QU, L., AZI, F., LIU, Y., LI, J., LV, X., DU, G., CHEN, J., CHEN, C.-H. & LIU, L. 2023 Recent progress in high-throughput droplet screening and sorting for bioanalysis. *Biosens. Bioelectr.* **225**, 115107.

SUN, X., ZHU, C., FU, T., MA, Y. & LI, H.Z. 2019 Breakup dynamics of elastic droplet and stretching of polymeric filament in a T-junction. *Chem. Engng Sci.* **206**, 212–223.

VERMA, N. & PANDYA, A. 2022 Challenges and opportunities in micro/nanofluidic and lab-on-a-chip. *Prog. Mol. Biol. Transl. Sci.* **186**, 289–302.

WANG, N., LIU, H. & ZHANG, C. 2016 Three-dimensional phase-field lattice Boltzmann model for incompressible multiphase flows. *J. Comput. Sci.* **17**, 340–356.

WANG, X., ZHU, C., WU, Y., FU, T. & MA, Y. 2015 Dynamics of bubble breakup with partly obstruction in a microfluidic T-junction. *Chem. Engng Sci.* **132**, 128–138.

WEI, B., HUANG, H., HOU, J. & SUKOP, M.C. 2018 Study on the meniscus-induced motion of droplets and bubbles by a three-phase lattice Boltzmann model. *Chem. Engng Sci.* **176**, 35–49.

WHITESIDES, G.M. 2006 The origins and the future of microfluidics. *Nature* **442**, 368–373.

XU, R., CHENG, Y., LI, X., ZHANG, Z., ZHU, M., QI, X., CHEN, L. & HAN, L. 2022 Aptamer-based signal amplification strategies coupled with microchips for high-sensitivity bioanalytical applications: a review. *Anal. Chim. Acta* **1209**, 339893.

XU, Z., LIU, H. & VALOCCHI, A.J. 2017 Lattice Boltzmann simulation of immiscible two-phase flow with capillary valve effect in porous media. *Water Resour. Res.* **53**, 3770–3790.

YAO, F., ZHU, P., CHEN, J., LI, S., SUN, B., LI, Y., ZOU, M., QI, X., LIANG, P. & CHEN, Q. 2023 Synthesis of nanoparticles via microfluidic devices and integrated applications. *Microchim. Acta* **190**, 1–21.

YU, Z. & FAN, L.-S. 2010 Multirelaxation-time interaction-potential-based lattice Boltzmann model for two-phase flow. *Phys. Rev.* E **82**, 046708.

ZHANG, J., CUI, H., LIU, H., CHEN, L., ZHANG, X. & LI, C. 2023*a* The surfactant role on a droplet passing through a constricted microchannel in a pressure-driven flow: a lattice Boltzmann study. *Langmuir* **39**, 13735–13747.

ZHANG, J., LIU, H. & BA, Y. 2019 Numerical study of droplet dynamics on a solid surface with insoluble surfactants. *Langmuir* **35**, 7858–7870.

ZHANG, J., LIU, H., WEI, B., HOU, J. & JIANG, F. 2021*a* Pore-scale modeling of two-phase flows with soluble surfactants in porous media. *Energy Fuels* **35**, 19374–19388.

ZHANG, J., LIU, H. & ZHANG, X. 2021*b* Modeling the deformation of a surfactant-covered droplet under the combined influence of electric field and shear flow. *Phys. Fluids* **33**, 042109.

ZHANG, J., SHEN, H., CUI, H., CHEN, L. & CHEN, L.G. 2023*b* The dynamic behavior of a self-propelled droplet on a conical fiber: a lattice Boltzmann study. *Phys. Fluids* **35**, 082119.

ZHANG, J., ZHANG, X., ZHAO, W., LIU, H. & JIANG, Y. 2022 Effect of surfactants on droplet generation in a microfluidic T-junction: a lattice Boltzmann study. *Phys. Fluids* **34**, 042121.

ZHU, P. & WANG, L. 2017 Passive and active droplet generation with microfluidics: a review. *Lab on a Chip* **17**, 34–75.

ZONG, Y., ZHANG, C., LIANG, H., WANG, L. & XU, J. 2020 Modeling surfactant-laden droplet dynamics by lattice Boltzmann method. *Phys. Fluids* **32**, 122105.

ZOU, L., HUANG, B., ZHENG, X., PAN, H., ZHANG, Q., XIE, W., ZHAO, Z. & LI, X. 2022 Microfluidic synthesis of magnetic nanoparticles in droplet-based microreactors. *Mater. Chem. Phys.* **276**, 125384.